Vascular regional analysis unveils differential responses to anti-angiogenic therapy in pancreatic xenografts through macroscopic photoacoustic imaging

Allison Sweeney[1], Andrew Langley[1], Marvin Xavierselvan[1], Ronak T. Shethia[1], Patrick Solomon[1], Aayush Arora[1], and Srivalleesha Mallidi[1,2 *]

[1]Department of Biomedical Engineering, Tufts University, Medford, MA, United States
[2] Wellman Center for Photomedicine, Massachusetts General Hospital, Boston, MA, United States

* Corresponding author: Srivalleesha Mallidi, Department of Biomedical Engineering, Tufts University, Medford MA 02155, srivalleesha.mallidi@tufts.edu

Keywords: pancreatic cancer, angiogenesis, sunitinib, vascular density, photoacoustics, endogenous contrast, vascular normalization

ABSTRACT

Background: Amongst the various imaging techniques that provide surrogate tumor radiographic indications to aid in planning, monitoring, and predicting outcomes of therapy, ultrasound-guided photoacoustic imaging (US-PAI) is a promising non-ionizing modality based on endogenous blood (hemoglobin) and blood oxygen saturation (StO_2) contrast. Adaptation of US-PAI to the clinical realm requires macroscopic system configurations for adequate depth visualization.

Methods: Here we present a vascular regional analysis (VRA) methodology of obtaining areas of low and high vessel density regions within the tumor (LVD and HVD respectively) by frequency domain filtering of macroscopic PA images. In this work, we evaluated the various vascular and oxygenation profiles of different murine xenografts of pancreatic cancer (AsPC-1, MIA PaCa-2, and BxPC-3) that have varying levels of angiogenic potentials and investigated the effects of receptor tyrosine kinase inhibitor (sunitinib) on the tumor microvessel density and StO_2.

Results: The administration of sunitinib resulted in transient deoxygenation and reduction in vessel density within 72 h in two (AsPC-1 and MIA PaCa-2) of the three tumor types. Utilizing VRA, the regional change in StO_2 (ΔStO_2) revealed the preferential targeting of sunitinib in LVD regions in only the AsPC-1 tumors. We also identified the presence of vascular normalization (validated through immunohistochemistry) in the sunitinib treated AsPC-1 tumors at day 8 post-treatment where a significant increases in HVD ΔStO_2 (~20%) were seen following the 72-hour time point, indicative of improved vessel flow and functionality. Treated AsPC-1 vasculature displayed increased maturity and functionality compared to non-treated tumors on day 8, while these same metrics showed no conclusive evidence of vascular normalization in MIA PaCa-2 or BxPC-3 tumors.

Conclusion: Overall, VRA as a tool to monitor treatment response allowed us to identify time points of vascular remodeling, highlighting its ability to provide insights into the tumor microenvironment for sunitinib treatment and other anti-angiogenic therapies.

Graphical Abstract

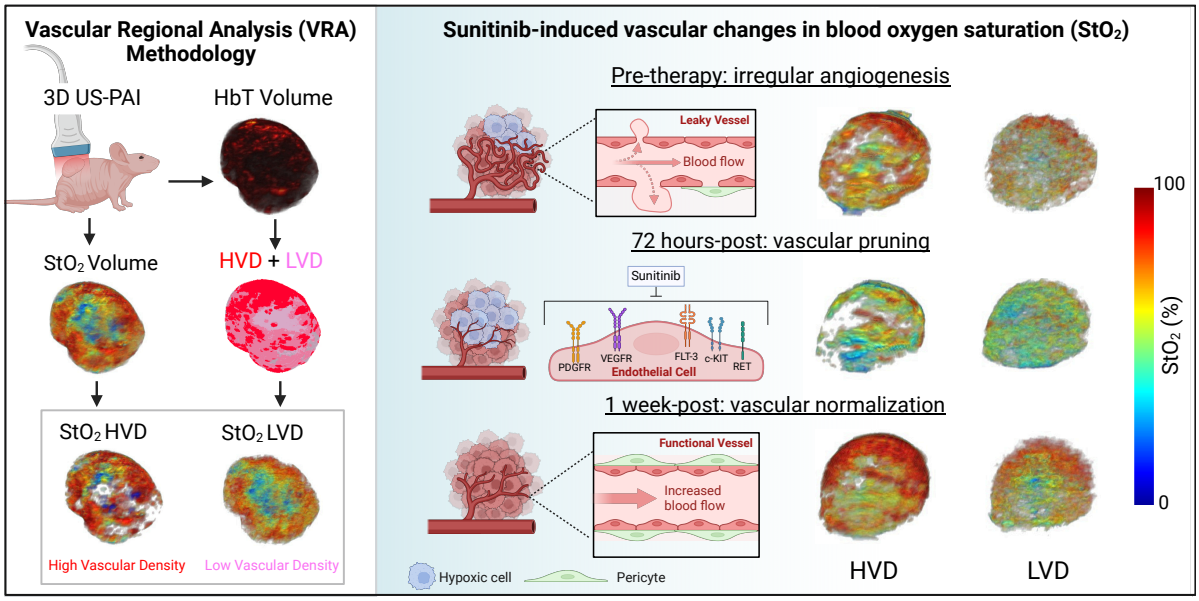

Introduction

Pancreatic cancer (PC) is the third leading cause of cancer-related deaths in the United States with a median survival time of 4.6 months and 5-year survival rate of 12% [1, 2]. Surgical resection coupled with systemic chemotherapy is currently the only curative treatment option for patients [3]. This poor prognosis can be attributed in part to the asymptomatic nature of PC that leads to late-stage detection, leaving only 10-20% of those diagnosed eligible for surgical resection [4]. Borderline-resectable PC must rely on preoperative therapy to shrink tumors prior to resection to improve surgical outcomes [5, 6] and neoadjuvant chemotherapy has been shown to increase survival, improve the chance of a full resection, and reduce the frequency of positive margins following surgery [4, 7]. Despite this, a considerable proportion of patients (~80%) with PC experience recurrence after undergoing resection and/or neoadjuvant chemotherapy, ultimately resulting in patient death [8, 9]. The biological factors underpinning the aggressive and treatment-resistant nature of PC can in part be attributed to features of the pancreatic tumor microenvironment (TME) [10]. The pancreatic TME is characterized by an abundance of stromal cells and extensive extracellular matrix, while remaining hypovascularized [10-12], resulting in a severely hypoxic TME which significantly influences tumor metabolism, therapeutic resistance, and angiogenesis [10, 12, 13]. Angiogenesis, the formation of new blood vessels, is a crucial element in the growth and spread of solid tumors. The irregular shape and function of tumor vasculature, may result in decreased blood flow and oxygenation, impeding the delivery of therapeutics to the tumor site [14-16].

Angiogenesis inhibitors are a family of therapeutics that act by suppressing the development of new blood vessels and recent research has shown that antiangiogenic treatment may be tailored to normalize tumor vasculature [17-19]. Vascular normalization employs modest doses with brief treatment durations to ameliorate the structural and functional irregularities of tumor blood vessels and sensitize tumor tissue to conventional therapy [17, 20-22]. Enhancing the uniformity of functional vascular density and improved configuration of arteries can lead to a decrease in regions of hypoxia and acidosis [17, 23-25]. In preclinical models, vascular normalization via anti-angiogenic therapies has been demonstrated to boost tumor blood supply and oxygenation [26-28], reduce metastatic burden [29, 30], and enhance the efficacy of ionizing radiation [31-34], chemotherapy [35-38], and immunotherapy [39-42]. The majority of antiangiogenic drugs target the vascular endothelial growth factor (VEGF) pathway, either by inhibiting VEGF-A with neutralizing antibodies or by blocking the VEGF-receptors (VEGFRs) with tyrosine kinase inhibitors (TKIs) [43-45]. Sunitinib is a multi-targeted TKI which utilizes the latter approach, inhibiting the activity of a number of tyrosine kinases, such as VEGFRs, platelet-derived growth factor receptors (PDGFRs), and stem cell factor receptors (KIT) [46, 47].

By inhibiting VEGFR, sunitinib limits endothelial cell proliferation and migration, ultimately decreasing overall vascular density in the tumor [48, 49]. The more organized and structurally stable vessels that may result from this process can enhance perfusion, but excessive inhibition can induce hypoxia and upregulate hypoxia inducible factors, complicating the tumor's vascular architecture [32, 47-69]. The inhibition of PDGFR works synergistically with VEGFR inhibition and its inhibition by sunitinib leads to inadequate pericyte coverage. This lack of coverage can result in a more permeable and less functional vasculature, further impacting hemodynamics and potentially leading to compromised tumor oxygenation [59, 70-72]. Sunitinib is authorized for the treatment of a variety of cancers, including renal cell carcinoma and gastrointestinal stromal tumors (GIST) such as PC [58, 65] Sunitinib remains the only targeted therapy currently approved for both GISTs and PCs, according to the NIH National Cancer Institute [73], highlighting its unique relevance in the context of this study. Much promise has been shown in administering sunitinib in combination with traditional treatments for PC as sunitinib has been demonstrated to make PCs more sensitive to radiation treatment *in vitro* and *in vivo* [66, 68]. Studies on combinatorial treatment have shown that the co-administration of sunitinib with gemcitabine in orthotopic PC models and nab-paclitaxel in subcutaneous PC models enhanced survival and reduced tumor burden compared to monotherapy [55, 69].

Although rapid innovations in cancer therapeutics have allowed for more targeted destruction of solid malignancies evaluating therapy response remains an obstacle, as there are limited endogenous radiographic indicators to aid in therapy planning and monitoring. Monitoring vascular structure and function is of particular interest, as these factors play a pivotal role in understanding therapy-induced changes in the TME [10, 12, 46]. Research into the functional indicators of therapy response in PC is critical for giving timely, accurate feedback on treatment efficacy and developing strategies for personalized medicine. Ultrasound-guided photoacoustic (PA) imaging (US-PAI) has received a lot of attention in recent years due to its non-invasive capacity to provide spatially co-registered anatomical, functional, and molecular data of the TME using endogenous contrast. PAI combines optical excitation and acoustic detection to generate high-resolution images containing functional information about biological tissues [74, 75]. PAI involves delivering nanosecond pulsed light into tissue, which is absorbed by chromophores and converted into heat causing thermoelastic expansion and contraction of the absorber and generation of acoustic waves detectable by US transducers [76, 77]. The minimal scattering of acoustic waves in biological tissues allows this hybrid modality to reap the benefit of increased penetration depth compared to purely optical techniques [74, 78]. Based on wavelength selection, US-PAI can display detailed functional and molecular information for a wide range of endogenous chromophores [79, 80]. The absorption spectra of hemoglobin changes when bound to oxygen, allowing the use of multi-wavelength PAI to assess blood oxygen saturation (StO_2) and hemoglobin concentration (HbT) by independently measuring oxyhemoglobin (HbO_2) and deoxyhemoglobin (Hb) distributions [81]. Among approaches used to image vasculature, PAI stands out for its exceptional scalability, making it suitable for imaging in the micro- to macroscopic scales. PAI has shown to be a promising modality to evaluate and monitor response to anti-angiogenic therapies based on changes in vascular morphology and StO_2, which are strongly associated with tumor hypoxia, according to preclinical investigations in murine models [82-85].

In addition to StO_2, microvessel density (MVD) has shown a correlation with aggressiveness in a variety of malignancies [86-89]. The emergence of tailored anti-angiogenic medication provides the possibility to use MVD analysis as both a prognostic and therapeutic marker. MVD can be measured with a variety of histological and *in vivo* imaging techniques, including PAI [89-92]. To our knowledge, the use of PAI to measure MVD *in vivo* has been mostly limited to PA microscopy (acoustic and optical resolution) or mesoscopy [92-100]. Microscopy techniques may attain far greater spatial resolution, but they are usually restricted to depths up to 1 mm [101]. In PAI specifically, mesoscopy refers to depths from 1-5 mm, with a resolution in the range of a few to tens of microns [100, 101]. In the push towards clinical translation of PAI, there comes the hurdle of balancing system resolution and penetration depth. Clinical imaging of tumors, specifically volumetric imaging, will require macroscopic configurations for adequate depth visualization. PA macroscopy encompasses depths exceeding 5 mm and offers resolution ranging from tens to hundreds of microns, in which individual microvessels cannot be resolved [102]. This illuminates the need for a surrogate marker to classify relative MVD within a tumor using macroscopic PAI. Herein, we investigate the feasibility of a surrogate imaging marker for vascular density in PC xenografts treated with sunitinib. We have chosen to utilize sunitinib as a proof of concept therapy because it has been shown to preferentially target immature vasculature and can induce vascular normalization in PC [32, 49]. We hypothesize that frequency domain filtering of macroscopic PA images will allow us to regionally classify high and low vascular density (HVD and LVD) areas and that our classification will show good agreement with the distribution of endothelial marker CD31. Utilizing vascular regional analysis (VRA) of treatment-induced StO_2 and HbT changes, we anticipate that sunitinib will preferentially reduce

StO_2 and HbT in LVD regions during early treatment time points, as sunitinib selectively prunes small vessels in PC [49]. Additionally, given the advent of vascular normalization, we will show the feasibility of VRA as a tool for identifying key time points of vascular remodeling in low-resolution macroscopic PAI configurations.

Materials and Methods

Cell lines and animal models

All animal studies in this work were approved by Tufts University's Institutional Animal Care and Use Committee (IACUC). Male homozygous Foxn1^{nu} nude mice (The Jackson Laboratory) were subcutaneously injected with 5 million AsPC-1, MIA PaCa-2, or BxPC-3 cells in 100 µL of Matrigel (50 µL of Matrigel + 50 µL of phosphate-buffered saline (PBS) using a 28-gauge insulin syringe. All cells were obtained from the American Type Culture Collection and supplemented with 10% fetal bovine serum and 1% penicillin-streptomycin (100 U/ml). BxPC-3 and MIA PaCa-2 cells were cultured in RPMI-1640 (Roswell Park Memorial Institute), while AsPC-1 was cultured in DMEM (Dulbecco's Modified Eagle Medium) media. All cells were grown in a T-75 flask and maintained in a humidified incubator at 37 °C and 5% CO_2. AsPC-1 and BxPC-3 cells were passaged 1-2 times each week, while MIA PaCa-2 cells were passaged 2-3 times per week.

Sunitinib treatment

The sunitinib solution was prepared at a concentration of 20 mg/mL by dissolving 200 mg of sunitinib L-malate (Sigma Aldrich) in 1 mL of dimethyl sulfoxide and 9 mL of corn oil. The solution was repeatedly vortexed and placed in a 50 °C ultrasonic water bath for intervals of 2 min each until no visible lumps or particles were present. The sunitinib solution was stored in 4 °C. Mice were treated with 80 mg/kg per day with sunitinib or vehicle for 20 days via oral gavage. The treatment regimen began once tumors reached a volume of approximately 50-150 mm^3. Mice were split into the following groups: Sunitinib group (MIA PaCa-2: n = 13; AsPC-1: n = 9; BxPC-3: n = 7) and no treatment (NT) group receiving 1x PBS (MIA PaCa-2: n = 11; AsPC-1: n = 8; BxPC-3: n = 5).

Longitudinal photoacoustic imaging

The experiment timeline is displayed in Figure 1 with image acquisition for each mouse starting once tumor volume reached a minimum of 50 mm^3. Pre-treatment imaging was performed 24 h before administration of the first dose (Day -1: D(-1)). Imaging during the treatment period was performed at precisely 24 and 72 h (Day 1: D(1) and Day 3: D(3)) after the first administered dose and continued thrice weekly (Day 6 and beyond: D(6+)). On D(3) post-treatment, 3 tumor specimens were extracted to utilize for validation of the VRA algorithm, deemed cohort #1. On D(8) post-treatment, 12 specimens were extracted from cohort #2 and histologically evaluated for AsPC-1 and MIA PaCa-2, with 6 total tumors from each cell line (3 per treatment group) to assess proliferation, vascular maturity, and perfusion. Mice euthanized on D(8) were injected with Tomato Lectin (TL) conjugated with DyLight® 488 (DL-1174-1, Vector Laboratories) 5-7 min before euthanasia. Cohort #3 encompassed the remaining mice and was longitudinally monitored with US-PAI through the last day of the treatment regimen (D(20)).

The Vevo LAZR-X (Fujifilm, VisualSonics) was used to capture US and PA images, utilizing the MX250S linear array transducer with a 6 dB bandwidth of 15-30 MHz, central transmit frequency of 21 MHz, axial resolution of 75 µm, and lateral resolution of 165 µm. The transducer was coupled to an integrated 20 Hz tunable laser (680-970 nm) via fiber optic cables. Throughout each of the imaging sessions, gain (22 dB for US, 45 dB for PAI) and persistence (20 averages per frame) remained constant. The Vevo LAZR-X Oxy-Hemo mode (750 and 850 nm laser pulses) was used to generate the PA images.

The imaging workflow was performed as follows. During the imaging session, mice were sedated with isoflurane (2-3% induction, 1.5% maintenance) with 100% oxygen gas and placed on a heating pad with ECG leads to monitor body temperature, heart rate, and breathing. To improve acoustic transmission between the transducer and the tumor during imaging, a bubble-free ultrasonic transmission gel (Aquasonic100 Ultrasonic Transmission Gel, Parker Laboratories, Inc.) was applied to the tumor. For each frame, an average of 20 images were captured at two wavelengths (750 and 850 nm), yielding a 2D PA image of tumor StO_2 in roughly 10 seconds. Each dual-wavelength

3D image of a tumor was acquired within 20 to 30 min, with the first imaging frame recorded at the back end of the mouse with each succeeding frame moving a 0.15 mm step toward the anterior.

Fluence compensation

Fluence compensation was performed using Monte Carlo simulations utilizing the Monte Carlo eXtreme (MCX) package for MATLAB [103, 104] and the PHotoacoustic ANnotation TOolkit for MATLAB (PHANTOM) [105]. Fluence compensation maps were generated for and applied to all PA images used in analysis. Briefly, 10 million photons (5 million from each fiber) were discharged from the light source toward the tissue volume. For every 0.1 mm^3 voxel inside the tissue volume, the optical characteristics of absorption coefficient, scattering coefficient, anisotropy factor, and refractive index were assigned dependent upon the tissue type in that area. Different optical properties were assigned for skin, soft tissue, and tumor tissue, which are summarized in Table S1. The localization and labeling of these tissue types within the volume were done utilizing the co-registered US images. In the simulation, water served as the interface between the light source and the tissue, to represent the ultrasound gel used as an acoustic coupling layer between the transducer and tissue. Photon propagation was maintained for 5 ns, which corresponds to the width of a common laser pulse used in PAI. Non-reflective boundary conditions were used throughout the simulation. As the transducer moves throughout the tumor volume to obtain a 3D scan, separate simulations were done for each transducer location and compiled to generate the resulting fluence map. More detailed information on the simulation geometry and parameters used for Monte Carlo parameters can be obtained from Sweeney et al [105].

Oxygen saturation and hemoglobin imaging via multi-wavelength PAI and spectral unmixing

The wavelength (λ) and depth (z) dependent photoacoustic initial pressure produced by pulsed light stimulation of optical absorbers, assuming stress confinement, may be represented by EQ. 1.

$$p_0(z,\lambda) = \Gamma\eta\mu_a(z,\lambda)\phi(z,\lambda) \quad (1)$$

Approximated as constants, Γ represents the Grüneisen parameter, and η represents the fraction of absorbed light converted into heat. The non-constant $\mu_a(z,\lambda)$ represents the optical absorption coefficient, and $\phi(z,\lambda)$ represents the light fluence. The absorption coefficient is simply the product of the molar extinction coefficient, $\epsilon(\lambda)$, and concentration, $C(z)$, of a specific chromophore. In the near-infrared (NIR) wavelength range, the absorption of water and lipids is negligible compared to hemoglobin and the mice imaged in this study had insignificant skin pigmentation, allowing us to ignore the contribution of melanin. With the assumption that hemoglobin is the primary biological absorber being imaged, EQ. 1 can be re-written as EQ. 2.

$$p_0(z,\lambda) = \Gamma[\epsilon_{Hb}(\lambda)C_{Hb}(z) + \epsilon_{HbO2}(\lambda)C_{HbO2}(z)]\phi(z,\lambda) \quad (2)$$

As the two wavelengths used in this study were $\lambda_1 = 750\,nm$ and $\lambda_2 = 850\,nm$, the molar concentrations of Hb ($C_{Hb}(z)$) and HbO_2 ($C_{HbO2}(z)$) were obtained by solving EQ. 3 with the non-negative linear least squares method. The molar concentration values of Hb and HbO_2 were input into EQ. 4 and EQ. 5 to calculate StO_2 and HbT respectively.

$$\begin{bmatrix} PA(z,\lambda_1) \\ PA(z,\lambda_2) \end{bmatrix} = \begin{bmatrix} C_{Hb}(z) \\ C_{HbO2}(z) \end{bmatrix} \begin{bmatrix} \epsilon_{Hb}(\lambda_1) & \epsilon_{HbO2}(\lambda_1) \\ \epsilon_{Hb}(\lambda_2) & \epsilon_{HbO2}(\lambda_2) \end{bmatrix} \quad (3)$$

$$StO_2 = \frac{C_{HbO2}(z)}{C_{Hb}(z) + C_{HbO2}(z)} \quad (4)$$

$$HbT = C_{Hb}(z) + C_{HbO2}(z) \quad (5)$$

Where $PA(z,\lambda)$ represents the fluence compensated PA image i.e. $PA(z,\lambda) = \frac{p_0(z,\lambda)}{\phi(z,\lambda)}$.

Image denoising

To improve the signal-to-noise (SNR) of the StO_2 images, the HbT images were analyzed to find a noise threshold. The noise threshold of each image was calculated by taking the average HbT signal from two 50x50 pixel ROIs and averaging this across each frame in the volumetric image. The maximum value for each mouse was then averaged across all mice for all time points (Table S2) and rounded to the nearest ten-thousandth to produce a generalized threshold to be applied to all images. If the HbT value of a particular voxel in the full volumetric image

was less than the specified threshold, the regions were considered to be avascular, and the corresponding pixel in the oxygen saturation matrix was set to zero and omitted from further analysis.

Vascular regional analysis (VRA)

To segment the PA images into regions of HVD and LVD, frequency domain filtering was applied to the volumetric HbT images acquired from spectral unmixing as described in section 2.4 of the text. For clarity, no Fourier analysis was performed on pre-beamformed or single-wavelength PA volumes. Volumetric HbT images were normalized to a range of [0,1] and are denoted as I(x,y,z). A 3D Fast Fourier Transform (FFT) was performed on I(x,y,z) to get F(u,v,w) in the Fourier space (EQ. 6) and rearranged by shifting zero-frequency components from the edges to the center of the matrix.

$$F(u,v,w) = \sum_{x=0}^{M-1}\sum_{y=0}^{N-1}\sum_{z=0}^{P-1} I(x,y,z)e^{-2\pi i\left(\frac{ux}{M}+\frac{vy}{N}+\frac{wz}{P}\right)} \tag{6}$$

A Gaussian high pass filter (HP) was applied by elementwise multiplication with F to get the filtered volume (F'(u,v,w)) as shown in EQ. 7. The high pass filter was utilized to remove the low-frequency components of the image, which we hypothesized would contain signal corresponding to regions of low vascular density.

$$F'(u,v,w) = HP(u,v,w) \odot F(u,v,w) \tag{7}$$

$$HP(u,v,w) = 1 - e^{\frac{-D^2(u,v,w)}{2{D_0}^2}} \tag{7.1}$$

$$where\ D(u,v,w) = \left(\left(u-\frac{M}{2}\right)^2 + \left(v-\frac{N}{2}\right)^2 + \left(w-\frac{P}{2}\right)^2\right)^{\frac{1}{2}},\ D_0 = 1.5 \tag{7.2}$$

The 3D inverse Fourier transform was used to transform F' back into the spatial domain (EQ. 8) after rearranging the zero-frequency components back to the edges of the image to get the filtered volume (I'(x,y,z)). The values from the filtered volume, I', were not used in any data analysis but rather used specifically to segment the relative areas of high vascular density.

$$I'(x,y,z) = \frac{1}{MNP}\sum_{x=0}^{M-1}\sum_{y=0}^{N-1}\sum_{z=0}^{P-1} F(u,v,w)e^{2\pi i\left(\frac{ux}{M}+\frac{vy}{N}+\frac{wz}{P}\right)} \tag{8}$$

To regionally segment the tumor, the tumor mask was applied to I', which was then binarized using a modified Otsu thresholding method for log-normal (LN) distributions [106, 107] to obtain a mask where the foreground represents regions of HVD as shown in EQ. 9. We chose to apply a modified version of Otsu's method for LN distributions as the high-pass filtering step resulted in the HbT intensity distribution changing from gamma to LN. For clarity, we are using thresholding in this context to segment the vascular areas of the tumor and not to omit any regions from the analysis.

$$Mask_{HVD} = \begin{cases} 0 & I'(x,y,z) * Mask_{Tumor} < Thresh_{Otsu-LN} \\ 1 & I'(x,y,z) * Mask_{Tumor} \geq Thresh_{Otsu-LN} \end{cases} \tag{9}$$

The complementary mask of LVD regions was obtained via subtraction of HVD from the tumor region of interest (ROI). The areas of the tumor considered to be avascular (AV) from the noise thresholding described in section 2.5 were not included in the LVD regions as shown in EQ. 10.

$$Mask_{LVD} = Mask_{Tumor} - Mask_{AV} - Mask_{HVD} \tag{10}$$

This process allowed the regional analysis of the StO_2 maps as shown in Figure 2. As the majority of the low-frequency image components were removed with filtering, no analysis was performed on the filtered HbT images. Instead, the filtered images were solely utilized to define the vascular regions, which were then applied to the non-filtered HbT and StO_2 images.

Immunohistochemistry

Sectioning and staining procedures

Post-euthanasia, tumors were surgically removed with the skin and then placed in optimal cutting temperature (OCT) compound (Tissue-Tek) in the same orientation as the B-scan US-PA images. The tumor tissue was carefully sliced into cryo-sections, each measuring 10 µm in thickness, using a cryotome, then securely affixed to glass microscope slides. The histological examination was conducted using the hematoxylin and eosin (H&E) staining method, as well as immunofluorescence (IF) staining, following a previously reported protocol [83]. Briefly, the cryo-sections were fixed in ice-cold acetone and methanol solution (1:1 v/v) for 10 min and then air dried for 30 min, followed by three consecutive 5-minute washes with 1x phosphate-buffered saline (PBS). The tissue sections were then blocked with a 1x concentration blocking solution (Blocker™ BSA; #37525, ThermoFisher Scientific™) for 1 hour at room temperature. The immunostaining of vasculature within the tumor sections was performed using two primary antibodies, namely the Mouse PECAM-1/cluster of differentiation 31 (CD31) Affinity Purified Polyclonal Ab (#AF3628, R&D Systems Inc) and Rabbit ACTA2/alpha-Smooth Muscle Actin (αSMA) Polyclonal Ab (#50-556-90, Fisher Scientific). Tissue sections adjacent to sections chosen for CD31 and SMA were used to stain for the apoptosis marker Ki-67 using the primary antibody Human Ki-67/MKI67 Antibody (#AF7617, R&D Systems Inc) The tissue sections were incubated overnight at 4°C with the antibodies at dilutions of 1:5, 1:1000, and 1:20 for CD31, αSMA, and Ki-67, respectively. The primary antibodies were washed off with three rinses of 1x PBS the next day. Secondary antibody Donkey Anti-Goat IgG NL637 Affinity Purified PAb for CD31 (#NL002, R&D Systems Inc), Donkey Anti-Rabbit IgG (#NL004, R&D Systems Inc) for αSMA, and Donkey Anti-Sheep IgG (#NL010, R&D Systems Inc) for Ki-67, all at a dilution of 1:200, were added to the tissue sections and incubated for 2 h at room temperature. After the incubation, the sections were rinsed in PBS and the nuclei were counterstained and mounted with Slowfade gold antifade mountant containing 4',6-diamidino-2-phenylindole (DAPI; #S36939, Invitrogen). The slides were imaged at a 20X magnification using EVOS M7000 (ThermoFisher Scientific™) fluorescence imaging system. The IF-stained slides were imaged at the same brightness for all intensities using appropriate filter cubes. Tumors extracted on D(3) were stained with only CD31, while tumors extracted on D(8) were stained with CD31, αSMA, and Ki-67.

Immunofluorescence correlation with photoacoustic images for VRA validation

To validate the vascular segmentation algorithm, histological evaluation was performed using the endothelial marker CD31 with a complementary DAPI stain. The corresponding PA cross-section was determined using fiducial markers from the US images and matched to the closest H&E section as previously described [108]. Prior to correlation, IF images were thresholded to a level where autofluorescence was negligible and the tumor region was segmented from the DAPI stain and applied to all IF images. The MATLAB 'regionprops' function was used to find the bounding box of the tumor region in the IF images and the complementary bounding box of the tumor region from US-PA images. After cropping all images to the size of their bounding box, the IF images were down sampled to the size of the US-PA images. Thirion's demons algorithm [109, 110] implemented via the MATLAB 'imregdemons' function was used to co-register the down-sampled IF tumor mask with the US-PA tumor mask and was visually confirmed. Once co-registered, 1 mm x 1 mm rectangular ROIs were drawn, covering the entire tumor region to correlate the average CD31 signal intensity with the fraction of HVD pixels in that same area. Average CD31 signal intensity was calculated as the sum of CD31 intensity in a region divided by the total number of pixels in the region. This parameter was directly correlated with the fraction of HVD pixels, calculated as the sum of pixels labeled as HVD divided by the total number of pixels in the region. For the correlation analysis, 1 cross-section was analyzed for 3 different tumors, giving 91 total ROIs, each containing relative amounts of LVD and HVD. To ensure that the segmentation method worked independently of tumor size, vascularity, and treatment regimen, the tumors analyzed all differed in volume (V = 83.9, 246.4, and 105.6 mm^3), vascular parameters (StO_2 avg = 53.2%, 81.1%, 58.4%), and encompassed both treatment groups (sunitinib, vehicle, sunitinib).

Immunofluorescence to examine cell proliferation

We utilized the Ki-67 stain to measure the relative amounts of cell proliferation between both cell lines and treatment conditions at D(8). For both AsPC-1 and MIA PaCa-2, we analyzed 3 different tumors with a minimum of 5 total sections for each treatment group. Any sections with apparent image artifacts were omitted from the analysis. All images were normalized and thresholded to a level where autofluorescence was negligible and the DAPI and Ki-67 images were binarized for quantification. We defined the Ki-67 or proliferation index as the ratio of Ki-67 positive to DAPI positive pixels ($Ki\text{-}67^+$ / $DAPI^+$) over the entire tumor region, which was segmented from the DAPI image.

Immunofluorescence to determine the extent of vascular normalization

To confirm that the VRA measurements of HVD StO_2 and HbT were indicative of vascular remodeling, we resected 3 tumors from each treatment group on D(8) and conducted histological analysis. To this end, we performed triple sequential staining of endothelial cells, pericytes, and perfusing vessels using CD31, αSMA, and TL respectively with a DAPI counterstain. For AsPC-1 and MIA PaCa-2 sections from 3 different tumors were analyzed with a minimum of 5 total sections from each treatment group. Sections were omitted from quantitative analysis if there was the presence of significant image artifacts. Before analysis, IF images were normalized and thresholded to a level where autofluorescence was negligible and the CD31, TL, and αSMA images were binarized for quantification. The vascular normalization index (VNI) was calculated as the ratio of αSMA positive to CD31 positive pixels (αSMA^+ / $CD31^+$) for the entire tumor region in each section and averaged. Vascular perfusion was quantified in the same way, as the ratio of lectin-positive pixels to CD31-positive pixels (TL^+ / $CD31^+$). The tumor region was segmented from the DAPI stain and applied to all channels for each specific section.

Statistical analysis

GraphPad Prism (La Jolla, CA) was utilized to execute all statistical analyses. Pearson correlation analysis (two-tailed) was performed to validate the vascular segmentation algorithm described above. The Pearson's correlation coefficient was calculated for each tumor individually and en masse. Pearson's correlation analysis was also performed between our histological and PA imaging metrics across all tumors quantified. Volume growth rates were calculated from the exponential fitting of the volume growth curves for each mouse. The fit growth rate value between groups was compared using the extra sum-of-squares F test. Growth rate values were omitted from the analysis in the case of poor fitting due to non-treatment effects ($R^2 < 0.6$). For statistical comparison between two groups with equal variance at a specific time point, an unpaired two-sample t-test was performed. When comparing two groups of unequal variances, Welch's t-test was performed. To statistically compare HVD with LVD parameters, a one-tailed paired t-test was conducted as we were looking to see if there was a significant change in one direction. When comparing more than two unpaired groups (NT and sunitinib treated) and two or more different cell lines (MIA PaCa-2, BxPC-3, AsPC-1), ordinary two-way ANOVA was utilized (Fisher's LSD Test). A p-value < 0.05 was considered statistically significant for all analyses.

Results

Validation of vascular segmentation algorithm with immunohistology

Qualitatively there is a strong visual resemblance between the US image and the H&E stain of a representative tumor as shown by the tumor shape and fiducial markers (Figure 3A, B, black arrows). The HbT image of the same frame (overlayed onto the US image) and the corresponding CD31 stain show excellent visual correlation (Figure 3C,D). The areas labeled as HVD regions (white arrows) match areas of high CD31 signal, whereas the areas labeled as LVD regions (yellow arrows) match the areas of low CD31 signal intensity. The correlation between the average CD31 amplitude within a region and the fraction of pixels labeled HVD for 3 representative tumors is shown in Figure 3E. Each point on the plots shown represents a 1 mm x 1 mm ROI. The data points and ROIs that correspond to each tumor are separately plotted in Figure S1 and the data points for LVD + AV Fraction plotted against average CD31 amplitude is provided in Figure S2. Pearson's correlation coefficient indicates a strong correlation between CD31 and HVD for each mouse ($r = 0.853, 0.704, 0.856$) and en masse ($r = 0.781$). The p-values for Pearson's r are listed in Table S3. The strong quantitative and qualitative correlation between the pixels labeled HVD and CD31 signal intensity across several tumors' points to the reliability and repeatability of the proposed vascular segmentation algorithm.

Effect of sunitinib on tumor growth in PC

Treatment with sunitinib greatly reduced tumor growth rate in both AsPC-1, MIA PaCa-2, and BxPC-3 xenografts as shown in Figure 4A, B and C respectively. A significant difference in tumor volume between the treated and control groups was apparent within 3, 6, and 11 days of treatment for AsPC-1, MIA PaCa-2, and BxPC-3 respectively. Applying an exponential fit to each treatment group reveals that for non-treated tumors, AsPC-1 ($k = 0.0463$) had a lower best-fit value for growth rate (k) than MIA PaCa-2 ($k = 0.0905$) and BxPC-3 ($k = 0.1006$) tumors,

even though non-treated AsPC-1 tumors reached a larger volume than MIA PaCa-2 by D(20). Our findings were consistent with several studies utilizing subcutaneous pancreatic xenografts, in which quantitative measures of tumor volume showed that AsPC-1 tumors grew larger than MIA PaCa-2[111, 112].

The difference between the average growth rate calculated for each cell line and treatment group is shown in Figure 4D and reveals that the average growth rates were significantly different between AsPC-1 and BxPC-3 treated tumors (p-value < 0.001) as well as AsPC-1 and MIA PaCa-2 treated tumors (p-value < 0.05). There was also a significant difference in the growth rate between sunitinib-treated and control tumors in AsPC-1 (p-value < 0.0001), MIA PaCa-2 (p-value < 0.0001), and BxPC-3 (p-value < 0.05) groups respectively. The growth rates of the non-treated tumors were insignificant between all cell lines (p-value > 0.05). The observed tumor volume changes throughout the treatment period are shown in Figure 4E. No significant difference was observed when comparing the three cell lines for the treated groups. Although the non-treated BxPC-3 tumors reached a significantly higher volume than both AsPC-1 ($\Delta\bar{x}$ = 343.6 mm^3, p-value < 0.001) and MIA PaCa-2 ($\Delta\bar{x}$ = 409.8 mm^3, p-value < 0.0001) tumors. Within the three different tumor types, the volume change was significantly higher for the control group compared to treated groups for AsPC-1 ($\bar{x}$ = 292.7 mm^3, p-value < 0.001), MIA PaCa-2 ($\Delta\bar{x}$ = 170.3 mm^3, p-value < 0.05), and BxPC-3 ($\Delta\bar{x}$ = 566.4 mm^3, p-value < 0.0001). Descriptive statistics reveal that treated AsPC-1 tumor volume was reduced by an average of 17.46 mm^3 (σ = 27.11 mm^3) and that tumor volume reduction due to sunitinib was consistent between mice. Alternatively, treated MIA PaCa-2 and BxPC-3 tumors showed an average volume increase of 38.69 mm^3 (σ = 53.71 mm^3) and 52.41 mm^3 (σ = 3.67 mm^3) during the sunitinib regimen with MIA PaCa-2 displaying a much larger variation in response.

Ki-67 is an established marker for cellular proliferation [113]. In an analysis of more than 500 resected clinical PC samples, Ki-67 was identified as an independent prognostic marker for overall survival and recurrence-free survival. Patients exhibiting low expression (Ki-67 index ≤ 30% or 0.3) demonstrated significantly greater overall survival compared to those with high expression levels (Ki-67 index > 30% or 0.3), irrespective of cellular differentiation [114]. Prior data, concentrating on PC, also found that elevated Ki-67 expression correlated with adverse pathological characteristics, such as poor tumor differentiation, high tumor grade, and the development of lymph node metastases [115, 116], and was an independent predictor of unfavorable disease-free survival and disease-specific survival outcomes in PC and had a strong correlation with tumor grade [116-118]. Leveraging the results of these studies, we examined the differences in Ki-67 expression in untreated and sunitinib treated AsPC-1 and MIA PaCa-2 tumors. In Figure 5, the stain shown in orange overlaid represents Ki-67, while the nuclear stain DAPI is shown in blue, for representative AsPC-1 (Figure 5A-B) and MIA PaCa-2 (Figure 5D-E) tumors. The Ki-67 index (Ki-67$^+$ / DAPI$^+$) was significantly higher in the non-treated tumors in both AsPC-1 ($\Delta\bar{x}$ = 0.29, p-value < 0.001) and MIA PaCa-2 ($\Delta\bar{x}$ = 0.31, p-value < 0.01) as shown in the bar graphs in Figure 5C and Figure 5F respectively. Of note, the average proliferation index of treated AsPC-1 ($\bar{x}$ = 0.19) and MIA PaCa-2 ($\bar{x}$ = 0.19) tumors fall into the low expression category from a clinical standpoint, while the non-treated groups fall in the high expression category. This data is corroborated with the findings of Liang et al [114].

Regional vascular response of pancreatic xenografts to sunitinib

AsPC-1 tumors

The treatment-induced StO_2 changes in the AsPC-1 tumors are displayed quantitatively and qualitatively in Figure 6A-H and Fig 6I respectively. Representative 2D cross sectional image (typically from the center of the tumor) and 3D maps of tumor StO_2 are shown for the same tumor across various time points on the top and bottom panel of Figure 6I respectively. The corresponding HbT data and images for the StO_2 images shown in Figure 6I are provided in Figure S3. The images depict ultrasound imaging in grayscale overlaid with pseudo colormap where blue is low oxygenated areas and red is highly oxygenated regions. When comparing average 3D StO_2 of the entire tumor volume in treated versus non-treated groups (Figure S4), the sunitinib group has lower StO_2 at 24 h or D(1) ($\Delta\bar{x}$ = -10.29%, p-value < 0.05) and at 72 h or D(3) post-treatment ($\Delta\bar{x}$ = -9.80%, p-value < 0.05). These findings align with previous work from our group that has shown these time points to be significant for StO_2 reduction in PC xenografts treated with the VEGF inhibitor cabozantinib [82]. Segmenting the tumor regions into areas of HVD and LVD revealed that sunitinib preferentially induced these StO_2 changes in LVD areas (Figure 6B) early in the treatment regimen. As seen in Figure 6A-C there was no significant difference in StO_2 or ΔStO_2 between the treated and non-treated tumors at 24 h post-treatment (D(1)) in HVD areas (Figure 6C,D) . The 2D and 3D images at this time point shown in Figure 6I

449 also depict similar HVD profiles. Alternatively, there was a strong significant difference between the StO_2 values of
450 the two treatment groups in LVD areas at the same time-point ($\Delta\bar{x}$ = -11.61%, p-value < 0.05). A significant difference
451 in StO_2 between the HVD and LVD areas was also seen at 24 h post-treatment in the sunitinib-treated group (p-value
452 < 0.001), whereas no s difference was seen between the vascular regions for the control tumors (Figure 6C, grey bars).
453
454 At the 72-hour post-treatment time point D(3), significant differences in StO_2 remain between the treated and
455 control group for LVD ($\Delta\bar{x}$ = -12.05%, p-value < 0.01) with HVD regions still showing no significant difference
456 (Figure 6E). Substantial changes in oxygen saturation (ΔStO_2) from pre-treatment values (D(-1)) were seen at time
457 points D(1), D(3), and D(8) respectively (Figs. 6D,F,H). The ΔStO_2 in LVD regions was significantly different between
458 treated to control tumors on D(1) ($\Delta\bar{x}$ = -13.33%, p-value < 0.05) and D(3) ($\Delta\bar{x}$ = -13.77%, p-value < 0.01). No
459 significant differences between the treatment groups were observed in HVD regions on D(1) or D(3). The HVD images
460 in 6I also depict the same where StO_2 in the HVD regions remained relatively high in both treated and untreated groups
461 at all time points. Additionally, significant differences were observed between the LVD and HVD regions only in the
462 sunitinib group within the first 24 h ($\Delta\bar{x}$ = -1.8%, p-value < 0.05) and 72 h ($\Delta\bar{x}$ = -3.66%, p-value < 0.01) of the
463 regimen. Upon visual inspection of Figure 6I, it can be observed that 1. the HVD regions are mainly localized to the
464 tumor periphery in both the treated and non-treated AsPC-1 tumors and 2. Sunitinib treatment caused significant StO_2
465 changes mostly in the LVD regions. Given these results, we believe that sunitinib is preferentially targeting LVD areas
466 within the first 72 h of the treatment regimen in AsPC-1 xenografts.
467
468 The key time points associated with treatment-induced StO_2 decrease were observed within the first 72 h of
469 the treatment regimen, however, we also examined the longer-term effect of sunitinib on tumor vasculature.
470 Specifically, drastic reoxygenation of the HVD regions was observed by D(6) in half of the treated tumors and by D(8)
471 in all but one treated tumor. The reoxygenation is visually apparent in Figure 6I images, particularly in the HVD
472 images that at D(8) sunitinib treated tumors have reoxygenated. The amount of reoxygenation that occurred between
473 D(-1) and D(8) was significant in HVD compared to LVD regions ($\Delta\bar{x}$ = 3.19% , p-value < 0.001). The HVD regions
474 in treated tumors showed increased D(8) StO_2 ($\Delta\bar{x}$ = 9.78%, p-value < 0.05) and ΔStO_2 ($\Delta\bar{x}$ = 8.70%, p-value < 0.05)
475 when compared to the control group (Figure 6G,H). Additionally, from D(3:8) the oxygenation status of HVD regions
476 increased by >20% on average in treated tumors, which can be clearly seen in the 2D and 3D images shown in Figure
477 6I. On the other hand, there was a minimal change in tumor StO_2 in the no-treatment group, despite the increase in
478 tumor volume during these timepoints as displayed by the 3D renders. No significant difference was seen in StO_2 and
479 ΔStO_2 for the LVD or HVD regions of control tumors at D(8), indicating that the reoxygenation is related to sunitinib-
480 induced vascular changes.
481
482 While StO_2 and ΔStO_2 are both excellent indicators of vascular changes within the TME [82-84, 119], we
483 also examined the regional changes in HbT to determine if the observed increase in StO_2 could be attributed to vascular
484 remodeling or cyclic changes in tumor oxygenation. The regional HbT changes throughout the D(-1:11) period are
485 shown in Figure S3, while the whole tumor HbT changes are quantified in Figure S4. Sunitinib-treated tumors had
486 significantly higher HVD HbT signal at D(6) ($\Delta\bar{x}$ = 6.43e-4 a.u., p-value < 0.05) and D(8) ($\Delta\bar{x}$ = 6.35e-4 a.u., p-value
487 < 0.05) compared to the vehicle group. No significant differences between the treatment groups were seen for HbT in
488 LVD regions at these time points. The change in HbT (ΔHbT) from D(-1:8) was also significantly different between
489 the treated and control tumors in HVD regions ($\Delta\bar{x}$ = 8.17e-4 a.u., p-value < 0.001), and showed that the average HVD
490 HbT increased from pre-treatment levels in the treated group, while decreasing in the control group. Given the
491 insignificant changes in hemoglobin content in LVD regions, and increase in HVD HbT and StO_2, the increased blood
492 content in HVD regions is indicative of improved blood flow and vessel functionality at this juncture.
493
494 These observations provide strong evidence that vascular normalization is occurring within the D(4:8)
495 window. From our observations, it seems highly likely that sunitinib initially led to a temporary decrease in tumor
496 StO_2 while vessels were ablated prior to the onset of vascular remodeling. We see evidence of the preferential ablation
497 of vessels in the LVD regions, indicating these regions housed more immature vessels. Once these immature vessels
498 are pruned, a subsequent increase in HVD StO_2 and HbT is observed, providing surrogate markers for tissue
499 reoxygenation and improved blood flow. These structural and functional changes occur more prominently in the HVD
500 regions indicating the remodeling of more mature vessels in response to the preferential pruning of vessels in the LVD
501 region. All of these observed changes are consistent with previous reports of vascular normalization [17, 23, 24, 51,
502 120], which we go on to histologically validate in further sections.
503
504 MIA PaCa-2 tumors

Next, we investigated the MIA PaCa-2 xenografts to determine if the preferential treatment of LVD regions by sunitinib in PC was cell-line dependent. The treatment-induced regional StO_2 changes in the MIA PaCa-2 tumors are quantitatively and quantitively displayed in Figure 7A-H, and Figure 7I respectively. The respective HbT images for the StO_2 images shown in Figure 7 are displayed in Figure S4. The average StO_2 of the whole tumor in treated and non-treated groups is significantly different at 72- h or D(3) post-treatment ($\Delta\bar{x}$ = -21.04%, p-value < 0.0001) in the MIA PaCa-2 tumors (Figure S5). Compared to AsPC-1, the initial drop in StO_2 is over 10% greater in the MIA PaCa-2 tumors.

Interestingly, performing regional analysis on these tumors reveals a distinct trend from AsPC-1, i.e., in the MIA PaCa-2 tumors, sunitinib is inducing StO_2 changes non-preferentially during early treatment time points. There was a no significant difference in StO_2 between the treated and control tumors at 24 h post-treatment (D(1)) in LVD areas, while there was a statistical difference in the HVD areas ($\Delta\bar{x}$ = -9.17%, p-value < 0.05) as shown in Figure 7A-C. However, this is not the case for the D(-1:1) ΔStO_2 in either region. By D(3) and D(6), there are significant differences between the StO_2 in the treated and control tumors in both LVD and HVD areas, indicating no significant regional trend was occurring. Reoxygenation also happened in the MIA PaCa-2 tumors after the early treatment period, however, this reoxygenation was more subtle. From D(3:8) we do observe reoxygenation in both the LVD and HVD regions of treated tumors, however, neither region reaches a StO_2 value above the pre-treatment baseline (Figure 7D,F,H), or a value greater than the control tumors at the same juncture (Figure 7C,E,G) . Although the non-treated MIA PaCa-2 tumors displayed differing StO_2 levels in the HVD and LVD regions, the changes in these regions over time were consistent. Also, HbT decreased in the HVD and LVD areas for all treated mice during this window, unlike in AsPC-1. Regional HbT values from the D(-1:11) treatment days are provided in Figure S5 and show no significant differences in HbT or ΔHbT between the sunitinib and control group at these time points. The whole tumor StO_2 and HbT values for the entire treatment duration can be found in Figure S4.

Several distinct differences between the AsPC-1 and MIA PaCa-2 tumors can be seen in the 2D and 3D images of StO_2 in Figure 6I and 7I. Firstly, the untreated MIA PaCa-2 tumors remained highly oxygenated at D(8), unlike AsPC-1. Despite the MIA PaCa-2 tumors having a larger decrease in StO_2 between D(-1) and D(3), the overall LVD StO_2 in the MIA PaCa-2 treated tumors remained substantially higher (~10%) than that of AsPC-1 treated tumors on D(3). Neither average HbT nor StO_2 in sunitinib-treated mice was significantly higher than the controls and these values did not increase beyond pre-treatment levels indicating no improvement in vascular function. For these reasons, it is unlikely that any vascular normalization occurred during this window in the sunitinib-treated MIA PaCa-2 tumors, which is further confirmed by histological analysis. The increase in StO_2 was relatively small and was only observed for a short period, leading us to believe it is more likely due to cyclic fluctuations in tumor StO_2. Towards understanding these effects, our future work will involve monitoring the tumors at more frequent time points during the treatment regimen to investigate the prevalence of short-term fluctuations in StO_2.

BxPC-3 tumors

The AsPC-1 and MIA PaCa-2 have relatively low pro-angiogenic potential for PC cell lines, prompting us to examine the effects of sunitinib on the BxPC-3 cell line, which has significantly higher expression of pro-angiogenic factors [121]. While the overall tumor StO_2 significantly decreased from D(-1:3) in both treated MIA PaCa-2 and AsPC-1, the treated BxPC-3 group did not display this initial drop in StO_2. Despite the LVD regions having significantly lower StO_2 and ΔStO_2 than HVD regions at D(1,3,8) in the treated group, none of the LVD or HVD StO_2 metrics were significantly different between treatment groups (Figure S6). From this we can garner that, while sunitinib impacted the oxygenation differently in LVD regions compared to HVD regions, these changes were not drastic enough for the StO_2 in either region to significantly deviate from the control. Additionally, ΔHbT (Figure S7) was not significant between treatment groups (sunitinib and control) or vascular regions (HVD and LVD). These results align with another study where BxPC-3 tumors treated with sunitinib did not have an increased hypoxia fraction compared to control mice [49]. Furthermore, high vascular variability was present in the non-treated BxPC-3 mice prior to treatment onset (StO_2 σ = 13.43%) compared to AsPC-1 (StO_2 σ = 5.22%) and MIA PaCa-2 (StO_2 σ = 7.46%). Alternatively, due to the higher pro-angiogenic potential of BxPC-3, a higher dose of sunitinib may be required to induce the preferential reduction of StO_2 in LVD regions at the time points we have investigated. This is further confirmed by the high IC-50 value of BxPC-3 cells treated with sunitinib *in vitro* reported by Liang et al [122].

Histological evaluation confirms sunitinib-induced vascular normalization in AsPC-1

To confirm if VRA could provide surrogate markers of vascular normalization successfully, we conducted histological staining of CD31, αSMA, and TL on the frozen tissue sections. In mature blood vessels, the coordination between pericyte coverage, as evidenced by αSMA staining, and endothelial integrity, as indicated by CD31 expression, improves vascular stability and functionality [52, 70]. Enhanced vessel permeability facilitates increased vascular perfusion by enabling a greater flux of plasma and its constituents, including nutrients and oxygen, into the surrounding tissue. This phenomenon can be quantitatively assessed using TL staining, a method that selectively binds to the glycoproteins on the luminal surface of endothelial cells, allowing for the visualization and measurement of vascular density and perfusion [123]. Figure 8 displays representative AsPC-1 (Figure 8A-B) and MIA PaCa-2 (Figure 8D-E) tumors with CD31 (red), αSMA (green), and DAPI (blue). The TL stain (green) is shown for the same tissue cross-sections are shown in Figure 8G,H and J,K for AsPC-1 and MIA PaCa-2 respectively. Supporting our PA data, the VNI ($\alpha SMA^+ / CD31^+$) was significantly higher in the treated tumors for only the AsPC-1 ($\Delta\bar{x} = 0.34$, p-value < 0.05) cell line (Figure 8C and Figure 8F respectively). The observation of increased vessel functionality is further reinforced by the increased $TL^+ / CD31^+$ ratio shown in the treated AsPC-1 vasculature compared to the control ($\Delta\bar{x} = 0.19$, p-value < 0.001). The MIA PaCa-2 tumors treated with sunitinib did display an increase in the average $TL^+ / CD31^+$ ratio, however this increase was statistically insignificant.

We also correlated both $\alpha SMA^+ / CD31^+$ and $TL^+ / CD31^+$ with two of our VRA PA metrics (D(-1:8) HVD ΔStO_2 or D(8) HVD fraction (Figure 8G-H, O-P)) to investigate their relationship to vessel maturity and perfusion. The $\alpha SMA^+ / CD31^+$ metric had good correlation with D(-1:8) HVD ΔStO_2 ($r = 0.642$, p-value < 0.05) and excellent correlation with D(8) HVD fraction ($r = 0.884$, p-value < 0.001) with treated AsPC-1 tumors showing higher average of D(-1:8) HVD ΔStO_2 and HVD fraction compared to both treated MIA PaCa-2 tumors and all untreated tumors. The $TL^+ / CD31^+$ metric showed a good correlation with D(-1:8) HVD ΔStO_2 ($r = 0.703$, p-value < 0.05) and HVD fraction ($r = 0.695$, p-value < 0.05). Significant increases in HVD StO_2 and HVD fraction in a tumor undergoing anti-angiogenic therapy could serve as prognostic markers of vascular normalization or provide insights into vessel maturity and functionality *in vivo.*

Vascular differences between pancreatic cancer cell lines

While the effect of sunitinib on tumor volume between the AsPC-1, MIA PaCa-2, and BxPC-3 cell lines was comparable (Figure 4), the regional effect on the vasculature of the three cell lines was markedly different. To understand the discrepancy in response seen, we investigated the baseline vascular characteristics of the tumors from these cell lines. As shown in Figure 9A there was a difference in the pre-treatment LVD Fraction of AsPC-1 and MIA-PaCa-2 (p-value < 0.01) with AsPC-1 tumors displaying a significantly higher fraction of LVD areas. When looking at the whole tumor volume, the pre-treatment HbT values between AsPC-1 and MIA PaCa-2 were also significantly different on D(-1) (Figure 9B, p-value < 0.05), while the pre-treatment StO_2 was different between all cell lines. Figure 9D displays that the StO_2 was higher in MIA PaCa-2 tumors than in BxPC-3 ($\Delta\bar{x} = 12.88\%$, p-value < 0.0001) and AsPC-1 ($\Delta\bar{x} = 17.16\%$, p-value < 0.01) with BxPC-3 StO_2 being slightly lower than AsPC-1 ($\Delta\bar{x} = -1.89\%$, p-value < 0.05). The pre-treatment StO_2 and HbT as well as the relative amounts of LVD regions in a tumor may pre-dispose it to vascular remodeling with sunitinib, leading us to investigate the relationship between these parameters and the VRA metrics displaying key vascular features. We correlated our pre-treatment parameters with our VRA metrics for vascular pruning from D(-1) to D(3) in LVD regions and improved vessel function from D(-1) to D(8) in HVD regions for all of the treated mice.

For all of the sunitinib-treated tumors, D(-1:3) LVD ΔHbT metric showed good correlation with both pre-treatment LVD Fraction (Figure 9D, $r = -0.578$, p-value < 0.01) and pre-treatment HbT (Figure 9E, $r = -0.648$, p-value < 0.0001. Pre-treatment StO_2 displayed a strong negative correlation with the LVD ΔStO_2 from D(-1) to D(3) (Figure 9F, $r = -0.762$, p-value <0.0001), indicating that tumors with higher pre-treatment StO_2, more LVD areas, and higher average HbT tended to undergo a more drastic reduction in oxygenation and HbT content in LVD regions in response to sunitinib. Interestingly, we observe that the D(-1:8) HVD metrics also displayed a negative relationship with pre-treatment LVD Fraction (Figure 9G, $r = -0.795$, p-value <0.00001), HbT (Figure 9H, $r = -0.700$, p-value < 0.0001), and StO_2 (Figure 9I, $r = -0.562$, p-value < 0.01), showing that the tumors with the lowest pre-treatment levels of these

metrics showed the largest increase of blood content and oxygen in HVD regions at D(8). From this, we can infer that the level of vascular remodeling occurring from D(-1:8) may directly relate to the initial level of vascular pruning from D(-1:3). We correlated both D(-1:3) LVD ΔStO_2 with D(-1:8) HVD ΔStO_2 and D(-1:3) LVD ΔHbT with D(-1:8) HVD ΔHbT to further understand the relationship between vascular pruning and vessel normalization in treated tumors. Interestingly when correlating the D(-1:3) LVD with D(-1:8) HVD metrics, the levels of microvascular pruning (D(-1:3) LVD ΔHbT) effects the change in functional vessel blood content (D(-1:8) HVD ΔHbT) more drastically ($r = 0.557$, p-value < 0.01) than the levels of microvascular deoxygenation (D(-1:3) LVD ΔStO_2) effect the D(-1:8) HVD ΔStO_2 transient reoxygenation ($r = 0.430$, p-value < 0.05). These positive relationships align with many reports of vascular normalization where tumors that do not undergo complete vascular annihilation are shown to develop more mature and functional vasculature [19, 24, 25, 51]. Moreover, these results also illuminate the need for more extensive studies needed to understand the role of pre-treatment hemodynamics on tumor response to anti-vascular therapies, and thereby personalize the treatment strategy for effective outcomes.

Discussion and Conclusion

Comprehensive knowledge of the microvascular alterations within a tumor in response to anti-angiogenic therapy is crucial for optimizing efficacy and predicting long-term effects. Several methodologies are currently employed for microvessel segmentation in endogenous contrast PAI such as threshold-based segmentation [96, 124], morphology-based segmentation [92, 93, 98, 125, 126], and deep learning-based segmentation [95, 99, 127, 128]. While these methodologies can directly measure MVD based on microvessel segmentation, they have only been applied to microscopic or mesoscopic imaging configurations [92-100, 124-129] that provide high resolution but lack sufficient penetration depth to enable 3D visualization in a clinical setting. This reiterates the need to develop vascular segmentation or classification methodologies which can be applied to macroscopic, relatively low resolution photoacoustic images. To this end, we successfully developed a methodology for VRA, which is specifically applicable to *in vivo* macroscopic 3D PA images. The VRA methodology is able to differentiate LVD and HVD areas within a tumor to serve as surrogate markers for relative MVD. The VRA methodology was validated with quantitative histological analysis which revealed significant positive correlation between regions labeled HVD and endothelial marker CD31 ($r = 0.695$). Once the reliability of VRA was confirmed, we investigated the feasibility of utilizing VRA for monitoring therapy response in solid tumors.

The segmentation methodology was utilized to perform regional analysis on murine pancreatic xenografts treated with the TKI sunitinib. Our findings show that sunitinib induced significant changes in the oxygenation of both AsPC-1 and MIA PaCa-2 xenografts within the first 72 h of the treatment regimen in agreement with previous literature investigating the effects of anti-angiogenic therapy on subcutaneous pancreatic xenografts [82]. Region-based analysis indicated that sunitinib preferentially reduced StO_2 in LVD regions in AsPC-1 tumors but not MIA PaCa-2 tumors. At 24 h and 72 h post-treatment, StO_2 was significantly different between treated and control tumors in only LVD regions for AsPC-1. At these junctures, we also observed significant differences in ΔStO_2 when comparing HVD and LVD regions within treated tumors that were not present in untreated tumors. This indicates that the discrepancies seen are due to preferential targeting by sunitinib rather than non-treatment effects. The administration of sunitinib to AsPC-1 xenografts resulted in transient deoxygenation and reduction in vessel density that occurred preferentially within LVD regions. This was followed by reoxygenation in all regions and an increase in blood volume in HVD regions between D(3) and D(8), indicating that the remaining blood vessels had improved functionality within the reoxygenation window. This was further proven through triple sequential staining of endothelial cells, pericytes, and perfusing vessels using CD31, αSMA, and TL, where treated AsPC-1 tumors displayed increased vascular maturity and perfusion compared to non-treated tumors on D(8). On the other hand, these same metrics showed no conclusive evidence of vascular normalization in MIA PaCa-2 tumors.

The impact of anti-angiogenic therapies on tumor StO_2 is a subject of ongoing debate. Several studies have shown sunitinib therapy to promote vascular normalization by reorganizing the growth of new blood vessels in tumors by removing dysfunctional vessels [32, 59, 66, 69]. This vascular remodeling can promote the reoxygenation of tumors, showing promise for combination with treatments such as radiation or photodynamic therapy, which require oxygen [130, 131]. Conversely, other studies have found that sunitinib treatment does not restore normal blood vessel structure and instead leads to hypoxia [49, 67]. Sunitinib-induced VEGFR inhibition reduces pathological vascular proliferation and enhances the structural integrity of blood vessels, while PDGFR inhibition decreases pericyte recruitment, which can initially exacerbate vessel dysfunction, leading to hypoxia [50, 63]. However, when vessels

are partially normalized through the controlled application of these inhibitors, a more optimal pericyte coverage can occur, leading to improvements in vessel stability, permeability, and perfusion [70, 71] as displayed in the AsPC-1 tumors. This homeostatic balance between endothelial cells and pericytes enhances oxygen and nutrient delivery to tumor tissues, as shown through VRA by the increased HVD StO_2 and HbT during the identified vascular normalization window.

The baseline vascular characteristics of the different tumor models hint towards the differential response of AsPC-1 to sunitinib compared to MIA PaCa-2. One of the most crucial pro-angiogenic factors in cancer is VEGF, which has two primary roles mediated by the kinase insert domain receptor (KDR) gene: promoting the growth of new blood vessels (angiogenesis) and increasing the permeability of blood vessels (vascular hyperpermeability)[132-134]. The gene effect scores for KDR and KIT are negative in both cell lines and lower in AsPC-1 (KDR: -0.300, KIT: -0.103) than MIA PaCa-2 (KDR: -0.231, KIT: -0.056), indicating higher dependency of VEGFR and KIT for cell growth in AsPC-1[135, 136], which could explain the finding that MIA PaCa-2 tumors display slightly poorer volumetric response compared to AsPC-1. The gene effect scores could not be found for BxPC-3 cell line. The observation that LVD fractions were significantly lower, and HbT was significantly higher in MIA PaCa-2 before treatment onset aligns with additional *in vitro* work showing higher expression of pro-angiogenic factors COX-2 [137] and VEGF [138] when compared directly with AsPC-1. Our results combined with the aforementioned *in vitro* work strongly imply that AsPC-1 tumors may promote less angiogenic activity and contain more immature microvasculature than MIA PaCa-2.

Selective destruction of immature blood vessels from anti-angiogenic therapy is a known phenomenon [87, 139], and preferential targeting of sunitinib displayed in AsPC-1 and MIA PaCa-2 could be due to the relative maturity of the microvessels in these regions. Investigation of the mechanisms behind the favorable targeting of specific vascular regions by sunitinib requires in-depth analysis that is beyond the scope of this work, but an important future direction. Quantitative assays that measure the level of vascular maturation pre-treatment could potentially indicate the vulnerability of the tumor's existing blood vessels to sunitinib and would be a logical next step in this work. One weakness of this study is that a subcutaneous model was used, which may not accurately reflect the biology of human PC as much as a genetically engineered mouse model, or orthotopic implantation [140, 141].

Overall, our study demonstrates the feasibility of using VRA in macroscopic US-PAI to monitor the vascular microenvironmental changes caused by TKI therapy. VRA coupled with macroscopic US-PAI has the potential to provide valuable insights for the evaluation of key time points in which anti-angiogenic therapy is promoting vascular normalization, and how the intratumoral vascular density affects this progression. An extensive amount of further study is needed in dose optimization of anti-vascular therapies as those that induce hypoxia may render tumors less responsive to the majority of conventional therapies, adding an obstacle to the successful implementation of combination therapies. The present research did not include any experiments that combined sunitinib treatment with radiation therapy or chemotherapy. Nevertheless, the differences between HVD and LVD areas highlight the importance of accounting for relative vascular density in measurements of tumor StO_2 and HbT, and the potential of VRA to provide additional prognostic markers of treatment response and to identify crucial time points in which angiogenesis inhibitors can work synergistically with traditional therapeutics, particularly for tumors with low pro-angiogenic potential.

Abbreviations

σ: standard deviation; $\Delta\bar{x}$: difference between means of two groups; αSMA: alpha smooth muscle actin; Ab: antibody; AV: avascular; CD31: cluster of differentiation 31; D(#): day #; DAPI: 4',6-diamidino-2-phenylindole; DMEM: Dulbecco's modified eagle medium; FFT: fast Fourier transform; GIST: gastrointestinal stromal tumor; Hb: deoxyhemoglobin; HbO_2: oxyhemoglobin; HbT: total hemoglobin content; HVD: high vascular density; IF: immunofluorescence; IFFT: inverse fast Fourier transform; IFP: interstitial fluid pressure; KIT: kinase insert domain receptor; LN: log-normal; LS: least squares; LVD: low vascular density; MCX: Monte Carlo extreme; MVD: microvessel density; NIR: near infrared; NT: no treatment; PA: photoacoustic(s); PAI: photoacoustic imaging; PBS: phosphate buffered saline; PC: pancreatic cancer; PDGF(R): platelet-derived growth factor (receptor); PHANTOM: photoacoustic annotation toolkit for MATLAB; ROI: region of interest; RPMI-1640: Roswell Park Memorial Institute; SEM: standard error of the mean; SNR: signal-to-noise ratio; StO_2: blood oxygen saturation; TKI: tyrosine kinase inhibitor; TL: tomato lectin; TME: tumor microenvironment; US: ultrasound; US-PAI: ultrasound-guided photoacoustic imaging; VEGF(R): vascular endothelial growth factor (receptor); VRA: vascular regional analysis;

Acknowledgments

The authors would like to acknowledge the members of the integrated Biofunctional Imaging and Therapeutics (iBIT) laboratory, specifically Dr. Christopher D. Nguyen, Deeksha Sankepalle, Skye A. Edwards, Brooke Bednarke, and Avijit Paul and for their useful discussions and support. Funding support from National Institutes of Health grants (S10OD026844, R21CA263694 and R01CA266701) is gratefully acknowledged.

Contributions

The authors confirm contribution to the paper as follows: conceptualization: S. Mallidi and A. Sweeney; investigation: A. Sweeney, A. Langley, P. Solomon, R. Shethia, A. Arora, M. Xavierselvan; formal analysis: A. Sweeney; data curation and visualization: A. Sweeney and S. Mallidi; draft manuscript preparation: A. Sweeney and S. Mallidi; critical revision of the article: A. Sweeney, M. Xavierselvan, and S. Mallidi; project administration and supervision: S. Mallidi; funding acquisition: S. Mallidi. All authors reviewed the results and approved the final version of the manuscript.

Competing Interests

Authors have no competing interests to declare

FIGURES

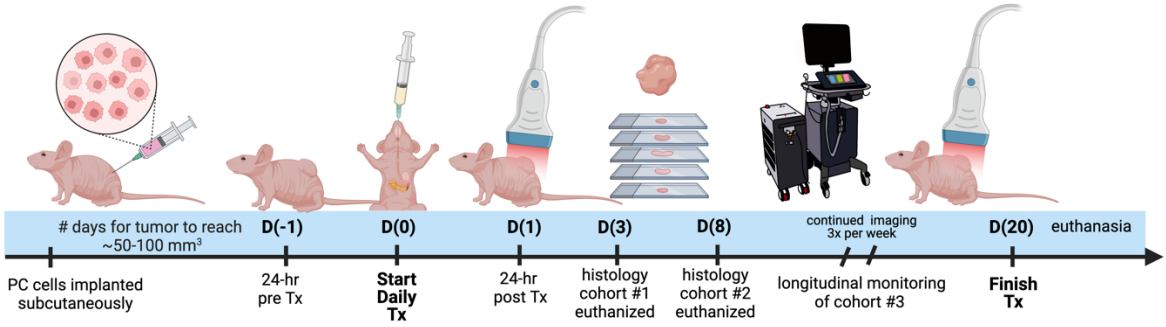

Figure 1. Study timeline describing the imaging, treatment, and histological examination of pancreatic tumor xenografts. D(0) represents Day 0, which is the day of the first treatment or vehicle administration. Cohort #1 was euthanized on D(3), cohort #2 was euthanized on D(8), and cohort #3 was monitored longitudinally up to D(20).

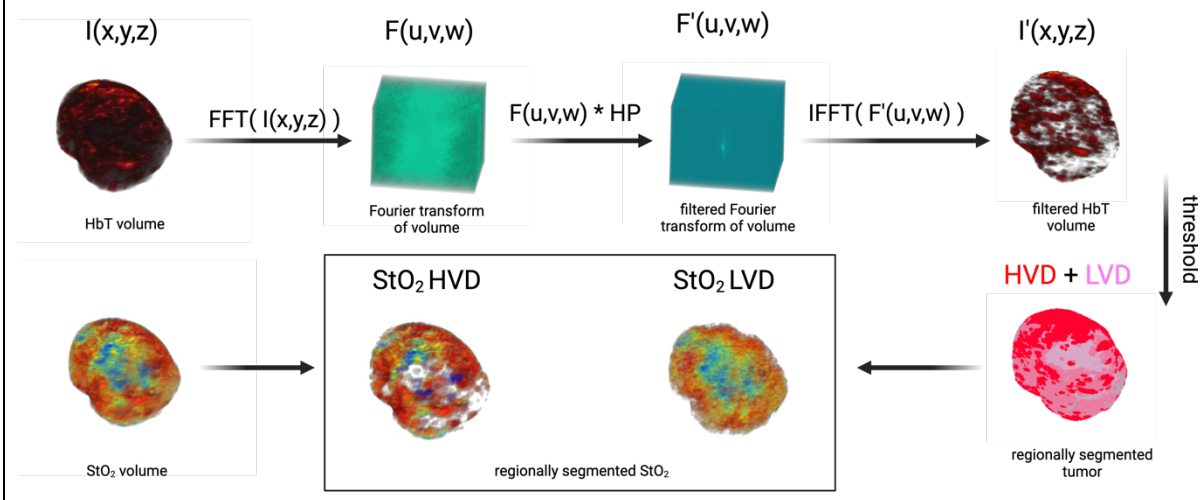

Figure 2. Image processing workflow displaying method for segmenting regions of high vascular density (HVD) and low vascular density (LVD)

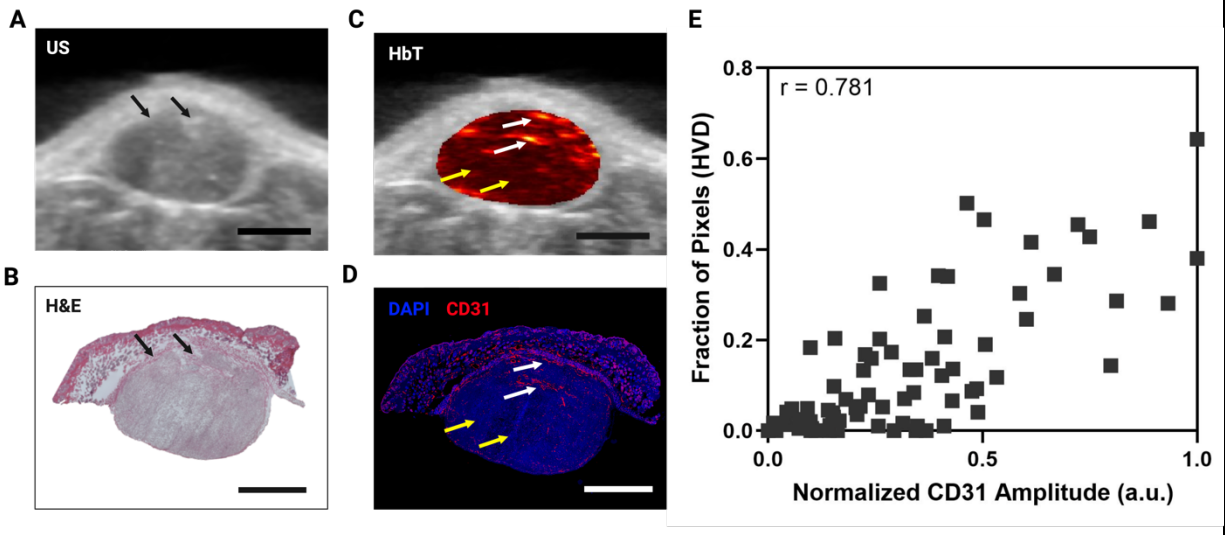

Figure 3. **A)** 2D cross sectional US image in a representative MIA PaCa-2 tumor. **B)** H&E stain of the same tumor cross section shown in A,C. **C)** 2D cross sectional image of HbT overlayed on US in a representative MIA PaCa-2 tumor with white arrows pointing towards areas of HVD and yellow arrows pointing towards areas of LVD. **D)** IF stain of the same tumor cross section shown in A,C with blue representing DAPI and red representing CD31. White arrows pointing towards areas of HVD and yellow arrows pointing towards areas of LVD according to the HbT image. **E)** Plot of normalized average CD31 intensity in a 1 mm x 1 mm ROI versus the fraction of pixels in the ROI labelled as HVD. All scale bars shown represent 2 mm.

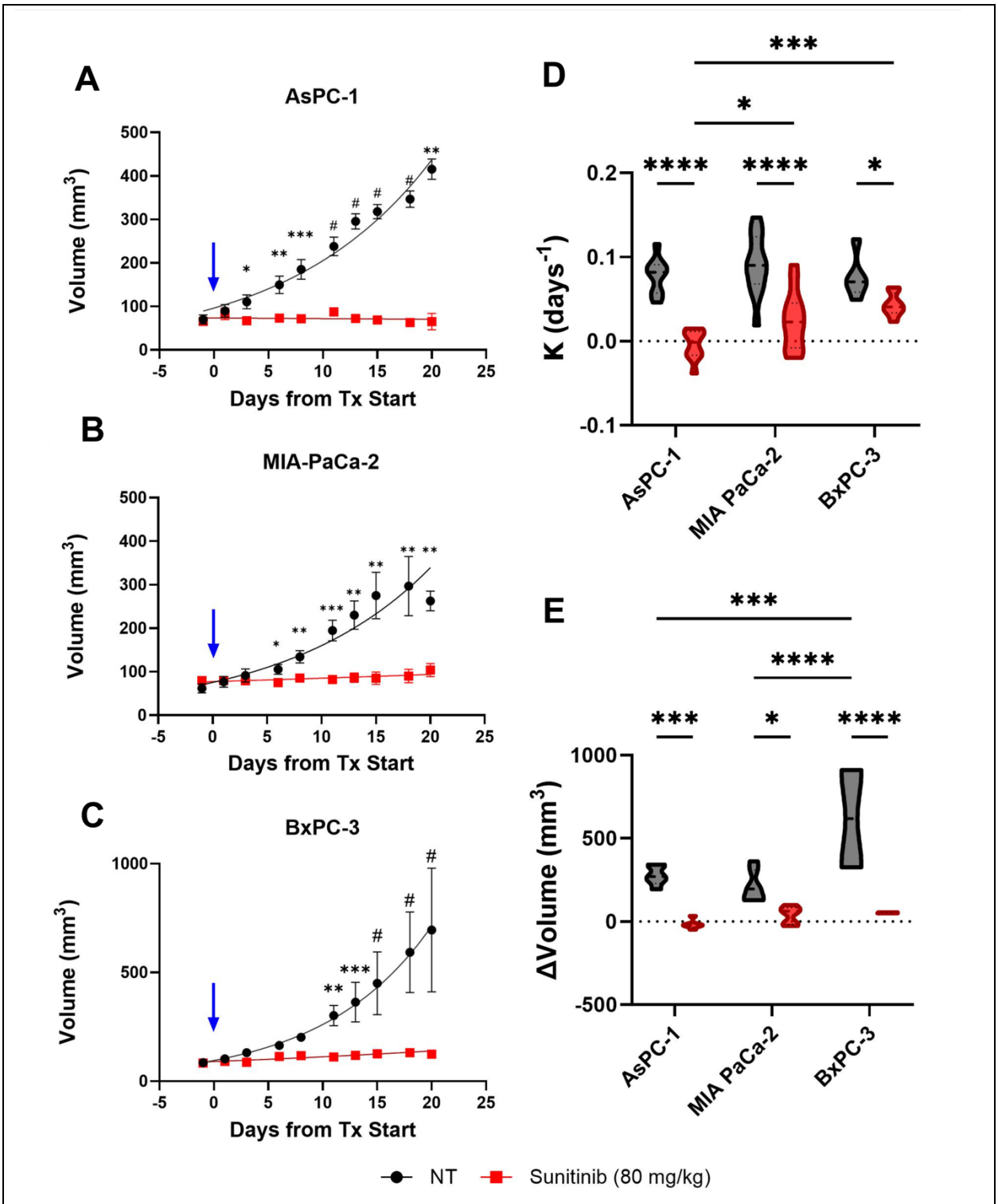

Figure 4. A-C) Plot of tumor volume for sunitinib (red) and no treatment - NT (black) groups for AsPC-1 (A), MIA PaCa-2 (B), and BxPC-3 (C) tumors with treatment starting at Day 0 (blue arrow). **D-E)** Violin plot of growth rate (D) and volume change from pre-treatment (D(-1)) to post-treatment or experiment end point (D(18-20)) (E) for sunitinib treated (red) and control tumors (black) in AsPC-1, MIA PaCa-2, and BxPC-3 tumors. All error bars shown represent SEM. p-values: * < 0.05, ** < 0.01, *** < 0.001, # or **** < 0.0001

748

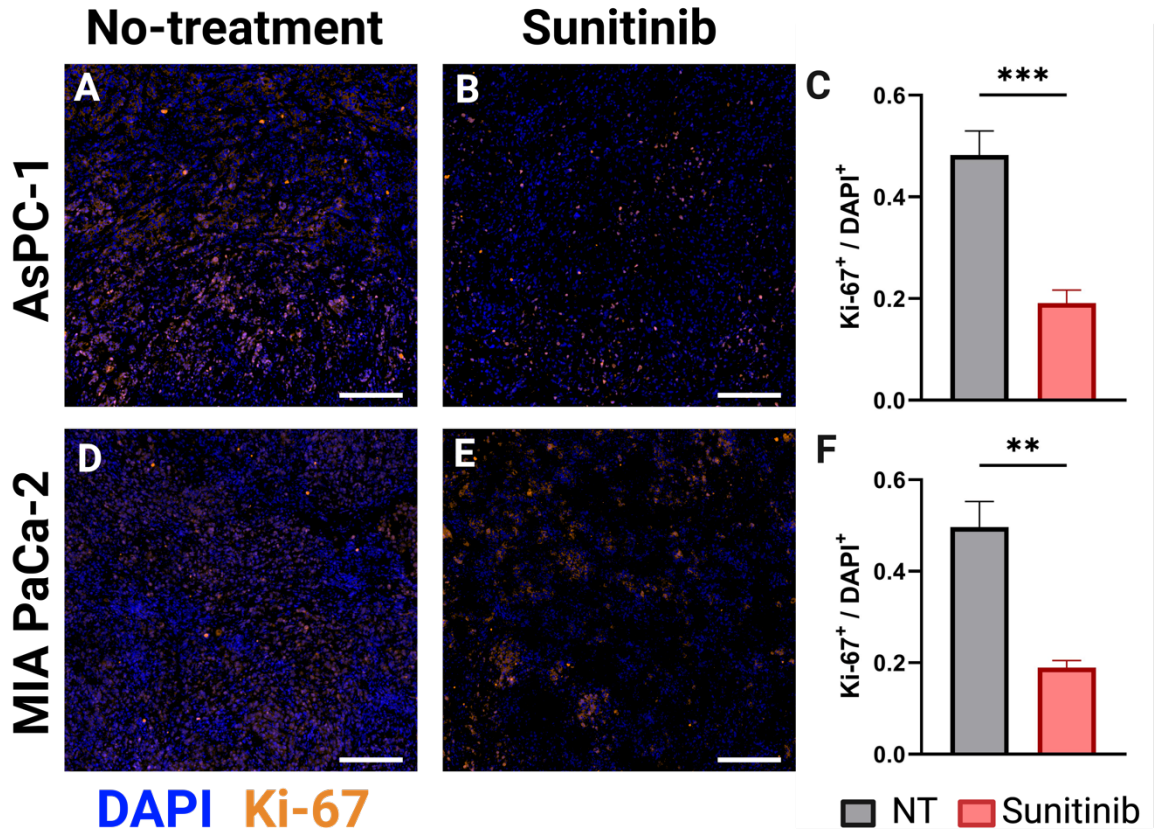

Figure 5. A-B) Representative AsPC-1 tumors stained for Ki-67 (orange) overlaid on DAPI (blue) for the control (NT) (A) and sunitinib treated (B) group. **C)** Bar graph comparing Ki-67$^+$ / DAPI$^+$ cell ratio between the control (black) and sunitinib (red) groups. **D-E)** Representative MIA PaCa-2 tumors stained for Ki-67 (orange) overlaid on DAPI (blue) for the control (D) and sunitinib treated (E) group. **F)** Bar graph comparing Ki-67$^+$ / DAPI$^+$ cell ratio between the control (black) and sunitinib (red) groups for MIA PaCa-2. All scale bars = 125 μm, All error bars shown represent SEM. p-values: * < 0.05, ** < 0.01, *** < 0.001

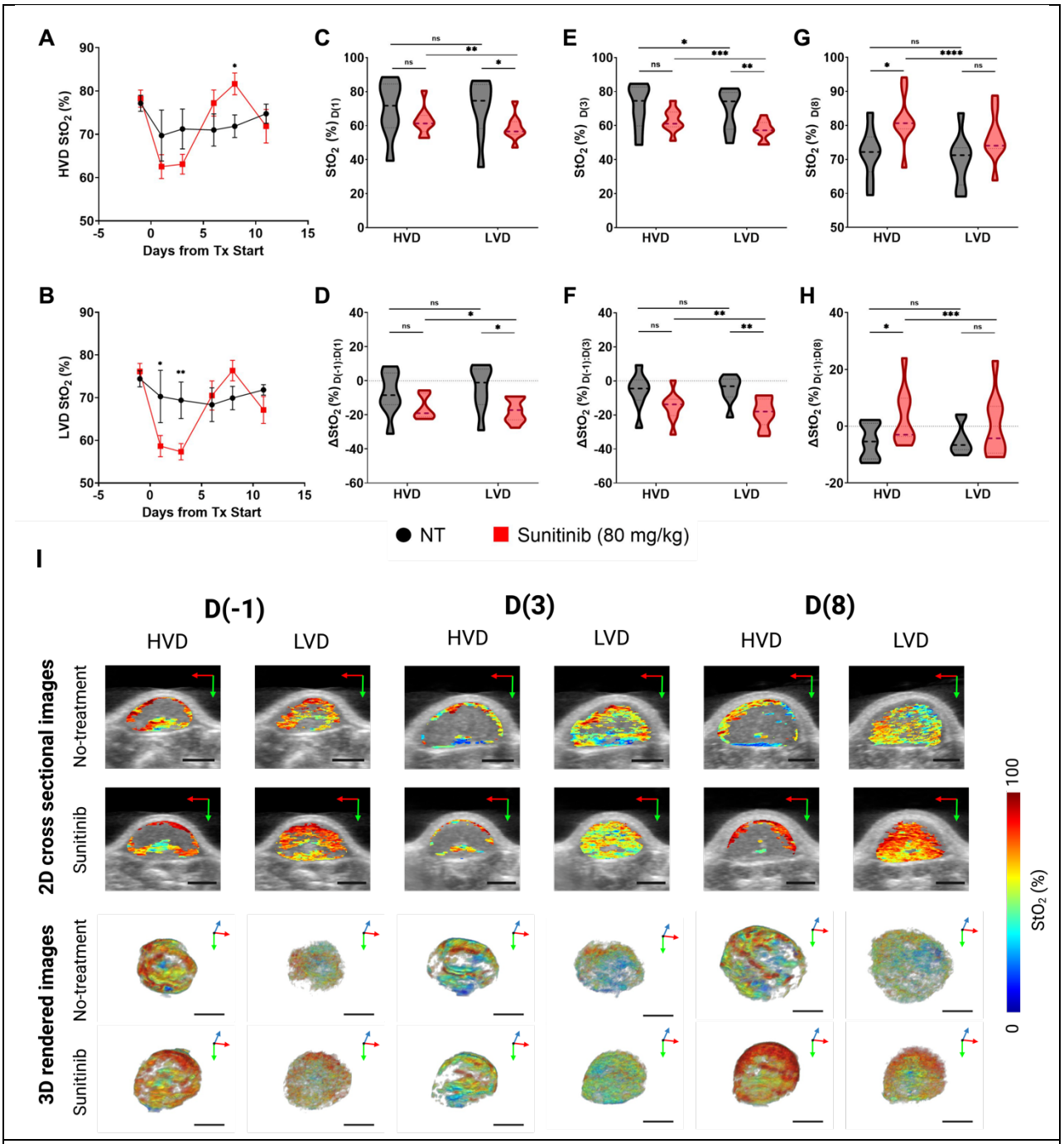

Figure 6. A-B) Plot of StO_2 in sunitinib (80 mg/kg) treated (red line) and untreated control (no treatment, black line) AsPC-1 tumors in regions of high vascular density (HVD) regions (A) and (LVD) regions (B). **C-D)** Violin plot comparing StO_2 on D(1) (C) and ΔStO_2 between D(1) and D(-1) (D) for Sunitinib at 80 mg/kg (red) and No Treatment (black) AsPC-1 tumors in areas HVD and LVD. **E-F)** Violin plot comparing StO_2 on D(3) (E) and ΔStO_2 between D(3) and D(-1) (F) for Sunitinib at 80 mg/kg (red) and No Treatment (black) AsPC-1 tumors in areas HVD and LVD. **G-H)** Violin plot comparing StO_2 on D(8) (G) and ΔStO_2 between D(8) and D(-1) (H) for Sunitinib at 80 mg/kg (red) and No Treatment (black) AsPC-1 tumors in areas HVD and LVD. **I)** Regional 2D cross sectional images (top) and 3D rendered images (bottom) of StO_2 in sunitinib (80 mg/kg) and no treatment AsPC-1 tumors displaying high HVD and LVD areas. All error bars shown represent SEM. Scale bars = 2 mm. p-values: * < 0.05, ** < 0.01, *** < 0.001, # or **** < 0.0001

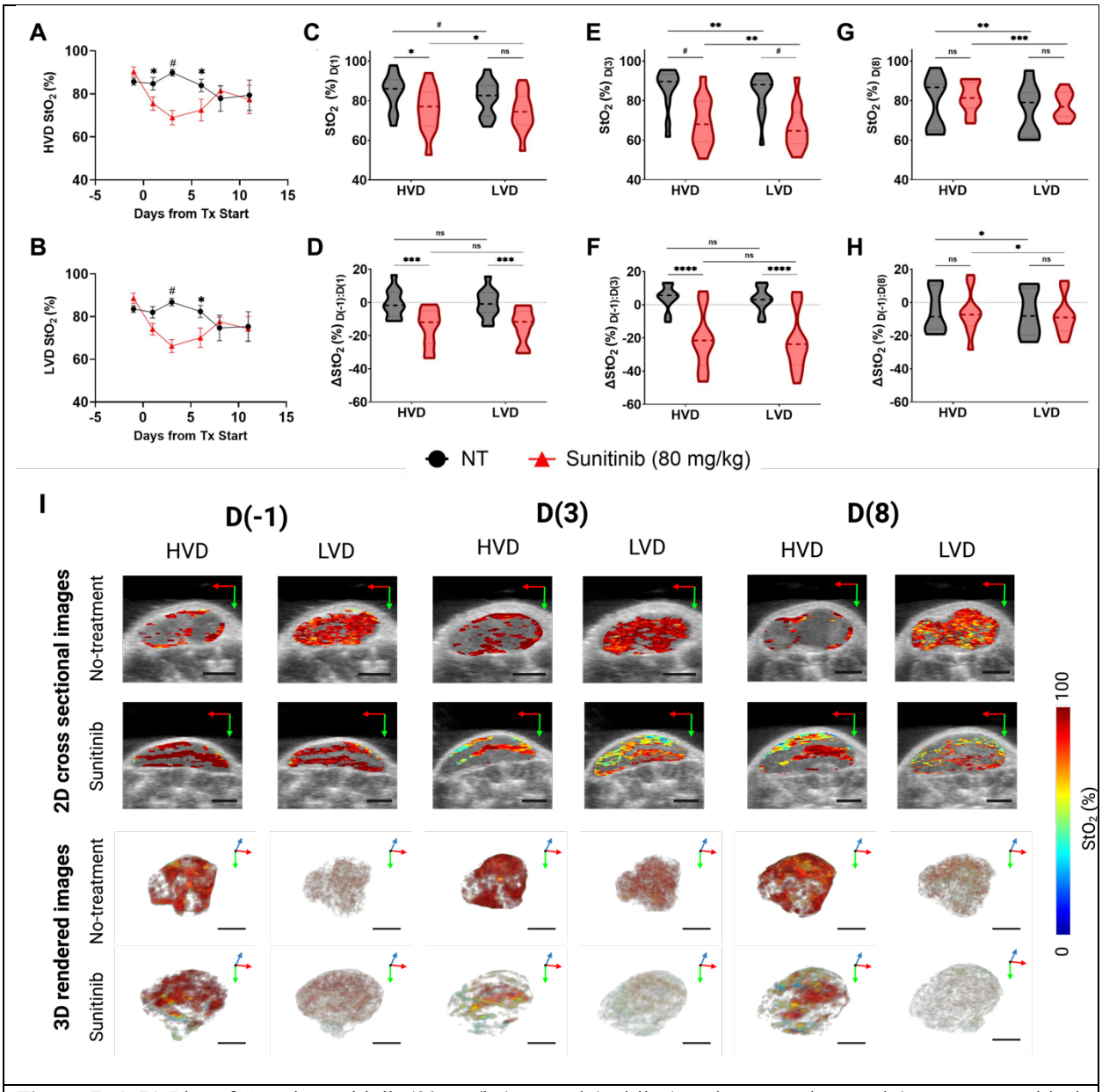

Figure 7. A-B) Plot of StO_2 in sunitinib (80 mg/kg) treated (red line) and untreated control (no treatment, black line) MIA PaCa-2 tumors in regions of high vascular density (HVD) regions (A) and (LVD) regions (B). **C-D)** Violin plot comparing StO_2 on D(1) (C) and ΔStO_2 between D(1) and D(-1) (D) for Sunitinib at 80 mg/kg (red) and No Treatment (black) MIA PaCa-2 tumors in areas HVD and LVD. **E-F)** Violin plot comparing StO_2 on D(3) (E) and ΔStO_2 between D(3) and D(-1) (F) for Sunitinib at 80 mg/kg (red) and No Treatment (black) MIA PaCa-2 tumors in areas HVD and LVD. **G-H)** Violin plot comparing StO_2 on D(8) (G) and ΔStO_2 between D(8) and D(-1) (H) for Sunitinib at 80 mg/kg (red) and No Treatment (black) MIA PaCa-2 tumors in areas HVD and LVD. **I)** Regional 2D cross sectional images (top) and 3D rendered images (bottom) of StO_2 in sunitinib (80 mg/kg) and no treatment MIA PaCa-2 tumors displaying high HVD and LVD areas. All error bars shown represent SEM. Scale bars = 2 mm. p-values: * < 0.05, ** < 0.01, *** < 0.001, # or **** < 0.0001

750

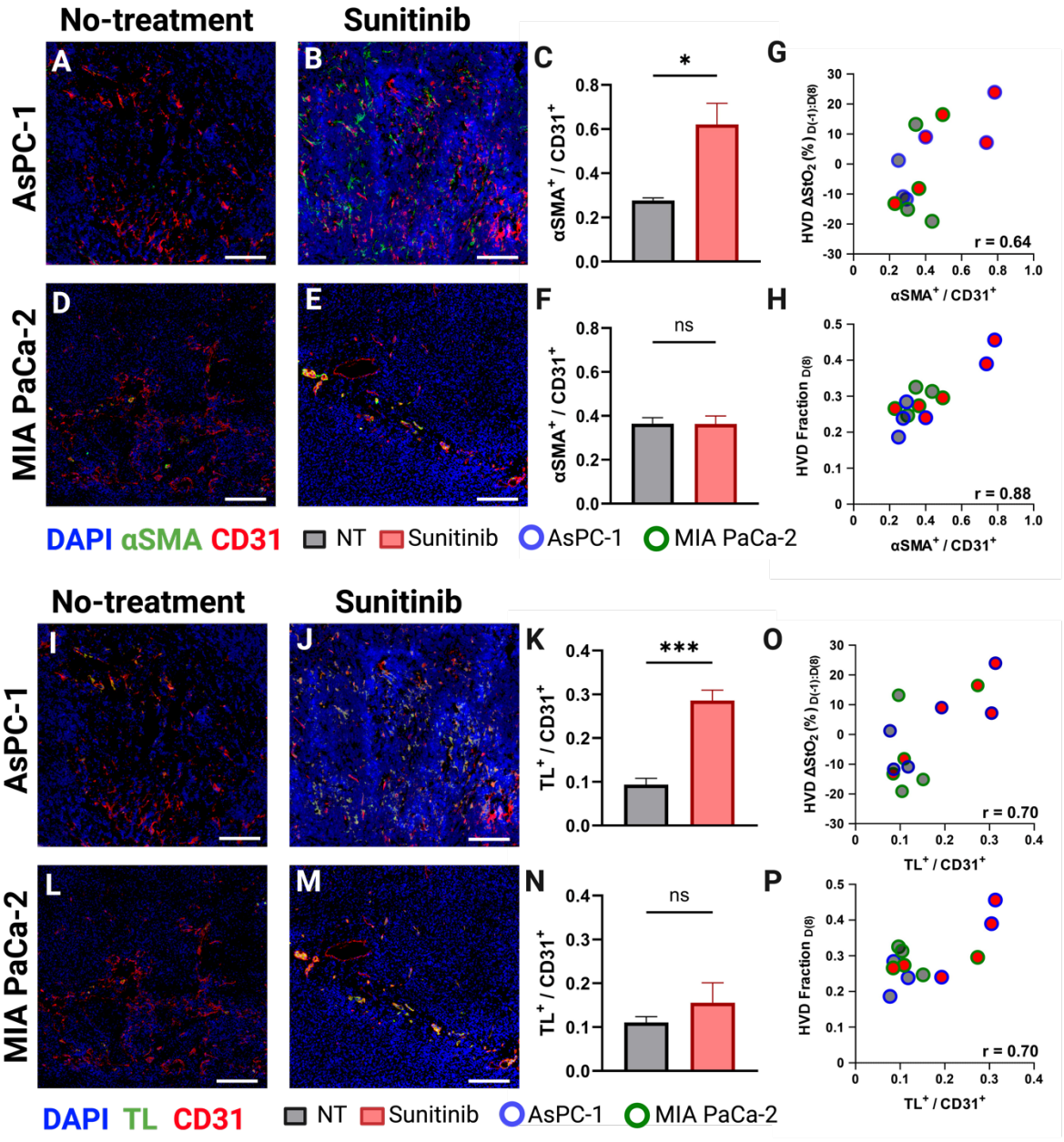

Figure 8. **A-B)** Representative AsPC-1 tumors stained for CD31 (red) and αSMA (green) overlaid on DAPI (blue) for the control (A) and sunitinib (B) treated group. **C)** Bar graph comparing αSMA^{+} / $CD31^{+}$ cell ratio between the control (black) and sunitinib (red) groups. **D-E)** Representative MIA PaCa-2 tumors stained with CD31 (red) and αSMA (green) overlaid on DAPI (blue) for the control (D) and sunitinib (E) treated group. **F)** Bar graph (Mean +/- SEM) comparing αSMA^{+} / $CD31^{+}$ cell ratio between the control (black) and sunitinib (red) groups for MIA PaCa-2. **G-H)** Scatter plot of αSMA^{+} / $CD31^{+}$ versus the HVD ΔStO_2 between D(8) and D(-1) (G) HVD fraction on D(8) (H) for each histological sample with points corresponding to MIA PaCa-2 tumors outlined in green, and AsPC-1 tumors outlined in blue. **I-J)** Representative AsPC-1 tumors stained for CD31 (red) and TL (green) overlaid on DAPI (blue) for the control (I) and sunitinib (J) treated group. **K)** Bar graph comparing TL^{+} / $CD31^{+}$ cell ratio between the control (black) and sunitinib (red) groups. L-**M)** Representative MIA PaCa-2 tumors stained with CD31 (red) and TL (green) overlaid on DAPI (blue) for the control (L) and sunitinib (M) treated group. **N)** Bar graph comparing TL^{+} / $CD31^{+}$ cell ratio between the control (black) and sunitinib (red) groups for MIA PaCa-2. **O-P)** Scatter plot of TL^{+} / $CD31^{+}$ versus the HVD ΔStO_2 between D(8) and D(-1) (O) HVD fraction on D(8) (P) for

each histological sample with points corresponding to MIA PaCa-2 tumors outlined in green, and AsPC-1 tumors outlined in blue. It is to be noted that all four stains DAPI, TL, αSMA and CD31 are performed on the same section. For display purposes we showed DAPI, TL, CD 31 and DAPI, αSMA and CD31 images separately.
All scale bars = 125 μm, All error bars shown represent SEM. p-values: * < 0.05, ** < 0.01, *** < 0.001

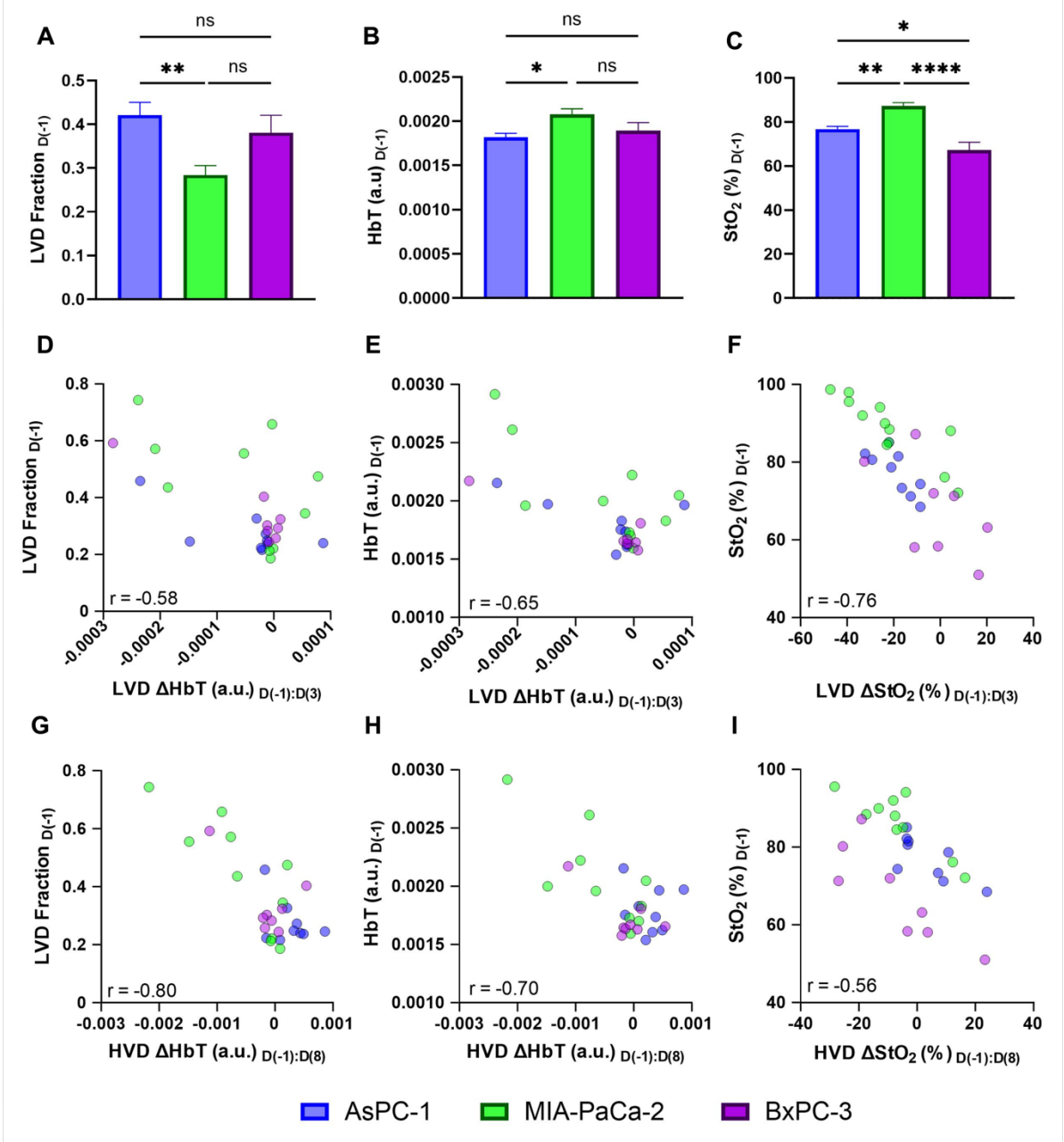

Figure 9. A-C) Bar graphs (Mean +/- SEM) comparing the pre-treatment LVD fraction **(A)**, HbT **(B)**, and StO_2 **(C)** in all AsPC-1 (blue) and MIA PaCa-2 (green) tumors and BxPC-3 (purple). **D-E)** scatter plots of LVD ΔHbT on D(3) versus pre-treatment LVD fraction (D), and HbT (E). **F)** scatter plot of LVD ΔStO_2 from D(-1) to D(3) in sunitinib-treated tumors.). G-**H)** scatter plots of HVD ΔHbT on D(8) versus pre-treatment LVD fraction (D), and HbT (E). **I)** scatter plot of HVD ΔStO_2 from D(-1) to D(8) in sunitinib-treated AsPC-1 (blue), MIA PaCa-2 (green), and BxPC-3 (purple) tumors.
p-values: * < 0.05, ** < 0.01, *** < 0.001, **** < 0.0001

References

1. Ryan DP, Hong TS, Bardeesy N. Pancreatic adenocarcinoma. New England Journal of Medicine. 2014; 371: 1039-49.
2. Siegel RL, Miller KD, Wagle NS, Jemal A. Cancer statistics, 2023. CA Cancer J Clin. 2023; 73: 17-48.
3. McGuigan A, Kelly P, Turkington RC, Jones C, Coleman HG, McCain RS. Pancreatic cancer: a review of clinical diagnosis, epidemiology, treatment and outcomes. World J Gastroenterol. 2018; 24: 4846-61.
4. Strobel O, Neoptolemos J, Jager D, Buchler MW. Optimizing the outcomes of pancreatic cancer surgery. Nat Rev Clin Oncol. 2019; 16: 11-26.
5. Oba A, Ho F, Bao QR, Al-Musawi MH, Schulick RD, Del Chiaro M. Neoadjuvant treatment in pancreatic cancer. Front Oncol. 2020; 10: 245.
6. Sutton JM, Abbott DE. Neoadjuvant therapy for pancreas cancer: past lessons and future therapies. World J Gastroenterol. 2014; 20: 15564-79.
7. Jang JY, Han Y, Lee H, Kim SW, Kwon W, Lee KH, et al. Oncological benefits of neoadjuvant chemoradiation with gemcitabine versus upfront surgery in patients with borderline resectable pancreatic cancer: a prospective, randomized, open-label, multicenter phase 2/3 rrial. Ann Surg. 2018; 268: 215-22.
8. Smith C, Zheng W, Dong J, Wang Y, Lai J, Liu X, et al. Tumor microenvironment in pancreatic ductal adenocarcinoma: Implications in immunotherapy. World J Gastroenterol. 2022; 28: 3297-313.
9. Luu AM, Belyaev O, Höhn P, Praktiknjo M, Janot M, Uhl W, et al. Late recurrences of pancreatic cancer in patients with long-term survival after pancreaticoduodenectomy. J Gastrointest Oncol. 2021; 12: 474-83.
10. Sherman MH, Beatty GL. Tumor microenvironment in pancreatic cancer pathogenesis and therapeutic resistance. Annu Rev Pathol. 2023; 18: 123-48.
11. Ho WJ, Jaffee EM, Zheng L. The tumour microenvironment in pancreatic cancer — clinical challenges and opportunities. Nature Reviews Clinical Oncology. 2020; 17: 527-40.
12. Tao J, Yang G, Zhou W, Qiu J, Chen G, Luo W, et al. Targeting hypoxic tumor microenvironment in pancreatic cancer. J Hematol Oncol. 2021; 14: 14.
13. Zhang Z, Ji S, Zhang B, Liu J, Qin Y, Xu J, et al. Role of angiogenesis in pancreatic cancer biology and therapy. Biomedicine & Pharmacotherapy. 2018; 108: 1135-40.
14. Folkman J. Angiogenesis. Annu Rev Med. 2006; 57: 1-18.
15. Jain RK. Barriers to Drug Delivery in Solid Tumors. Scientific American. 1994; 271: 58-65.
16. Potente M, Gerhardt H, Carmeliet P. Basic and therapeutic aspects of angiogenesis. Cell. 2011; 146: 873-87.
17. Goel S, Wong AH, Jain RK. Vascular normalization as a therapeutic strategy for malignant and nonmalignant disease. Cold Spring Harb Perspect Med. 2012; 2: a006486.
18. Zhou HC, Chen N, Zhao H, Yin T, Zhang J, Zheng W, et al. Optical-resolution photoacoustic microscopy for monitoring vascular normalization during anti-angiogenic therapy. Photoacoustics. 2019; 15: 100143.
19. Viallard C, Larrivée B. Tumor angiogenesis and vascular normalization: alternative therapeutic targets. Angiogenesis. 2017; 20: 409-26.
20. Jain RK. Normalization of tumor vasculature: an emerging concept in antiangiogenic therapy. Science. 2005; 307: 58-62.
21. Jain RK. Molecular regulation of vessel maturation. Nature Medicine. 2003; 9: 685-93.
22. Yang T, Xiao H, Liu X, Wang Z, Zhang Q, Wei N, et al. Vascular normalization: a new window opened for cancer therapies. Front Oncol. 2021; 11: 719836.
23. Goel S, Duda DG, Xu L, Munn LL, Boucher Y, Fukumura D, et al. Normalization of the vasculature for treatment of cancer and other diseases. Physiol Rev. 2011; 91: 1071-121.
24. Matuszewska K, Pereira M, Petrik D, Lawler J, Petrik J. Normalizing tumor vasculature to reduce hypoxia, enhance perfusion, and optimize therapy uptake. Cancers (Basel). 2021; 13.
25. Martin JD, Seano G, Jain RK. Normalizing function of tumor vessels: progress, opportunities, and challenges. Annual Review of Physiology. 2019; 81: 505-34.
26. Lee C-G, Heijn M, di Tomaso E, Griffon-Etienne G, Ancukiewicz M, Koike C, et al. Anti-vascular endothelial growth factor treatment augments tumor radiation response under normoxic or hypoxic conditions. Cancer Research. 2000; 60: 5565-70.
27. Eichhorn ME, Strieth S, Luedemann S, Kleespies A, Noth U, Passon A, et al. Contrast enhanced MRI and intravital fluorescence microscopy indicate improved tumor microcirculation in highly vascularized melanomas upon short-term anti-VEGFR treatment. Cancer Biology & Therapy. 2008; 7: 1006-13.

807 28. Cham KKY, Baker JHE, Takhar KS, Flexman JA, Wong MQ, Owen DA, et al. Metronomic gemcitabine
808 suppresses tumour growth, improves perfusion, and reduces hypoxia in human pancreatic ductal adenocarcinoma.
809 British Journal of Cancer. 2010; 103: 52-60.
810 29. Mazzone M, Dettori D, de Oliveira RL, Loges S, Schmidt T, Jonckx B, et al. Heterozygous deficiency of
811 PHD2 restores tumor oxygenation and inhibits metastasis via endothelial normalization. Cell. 2009; 136: 839-51.
812 30. Cui J, Che Z, Zou L, Chen D, Xie Z, Ding K, et al. JP1 normalizes tumor vasculature to suppress metastasis
813 and facilitate drug delivery by inhibiting IL-8. JCI Insight. 2023; 8.
814 31. McGee MC, Hamner JB, Williams RF, Rosati SF, Sims TL, Ng CY, et al. Improved intratumoral oxygenation
815 through vascular normalization increases glioma sensitivity to ionizing radiation. International Journal of Radiation
816 Oncology*Biology*Physics. 2010; 76: 1537-45.
817 32. Batra S, Matsumoto S, Hyodo F, Mitchell J, Krishna MC. MRI assessment of angiogenesis inhibitor
818 sunitinib's influence on tumor oxygenation to identify an optimal chemoradiotherapeutic window. International
819 Journal of Radiation Oncology*Biology*Physics. 2009; 75: S43.
820 33. Dings RP, Loren M, Heun H, McNiel E, Griffioen AW, Mayo KH, et al. Scheduling of radiation with
821 angiogenesis inhibitors anginex and Avastin improves therapeutic outcome via vessel normalization. Clin Cancer Res.
822 2007; 13: 3395-402.
823 34. Jiang S, Zhou Y, Zou L, Chu L, Chu X, Ni J, et al. Low- dose Apatinib promotes vascular normalization and
824 hypoxia reduction and sensitizes radiotherapy in lung cancer. Cancer Medicine. 2023; 12: 4434-45.
825 35. Zhao Z, Shuang T, Gao Y, Lu F, Zhang J, He W, et al. Targeted delivery of exosomal miR-484 reprograms
826 tumor vasculature for chemotherapy sensitization. Cancer Letters. 2022; 530: 45-58.
827 36. Tong RT, Boucher Y, Kozin SV, Winkler F, Hicklin DJ, Jain RK. Vascular normalization by vascular
828 endothelial growth factor receptor 2 blockade induces a pressure gradient across the vasculature and improves drug
829 penetration in tumors. Cancer Research. 2004; 64: 3731-6.
830 37. Weiss A, Bonvin D, Berndsen RH, Scherrer E, Wong TJ, Dyson PJ, et al. Angiostatic treatment prior to
831 chemo- or photodynamic therapy improves anti-tumor efficacy. Scientific Reports. 2015; 5: 8990.
832 38. Segers J, Fazio VD, Ansiaux R, Martinive P, Feron O, Wallemacq P, et al. Potentiation of cyclophosphamide
833 chemotherapy using the anti-angiogenic drug thalidomide: Importance of optimal scheduling to exploit the
834 'normalization' window of the tumor vasculature. Cancer Letters. 2006; 244: 129-35.
835 39. Zhao S, Ren S, Jiang T, Zhu B, Li X, Zhao C, et al. Low-dose apatinib optimizes tumor microenvironment
836 and potentiates antitumor effect of PD-1/PD-L1 blockade in lung cancer. Cancer Immunology Research. 2019; 7: 630-
837 43.
838 40. Li B, Lalani AS, Harding TC, Luan B, Koprivnikar K, Huan Tu G, et al. Vascular endothelial growth factor
839 blockade reduces intratumoral regulatory T cells and enhances the efficacy of a GM-CSF–secreting cancer
840 immunotherapy. Clinical Cancer Research. 2006; 12: 6808-16.
841 41. Yi M, Jiao D, Qin S, Chu Q, Wu K, Li A. Synergistic effect of immune checkpoint blockade and anti-
842 angiogenesis in cancer treatment. Molecular Cancer. 2019; 18: 60.
843 42. Georganaki M, van Hooren L, Dimberg A. Vascular targeting to increase the efficiency of immune checkpoint
844 blockade in cancer. Front Immunol. 2018; 9: 3081.
845 43. Qin S, Li A, Yi M, Yu S, Zhang M, Wu K. Recent advances on anti-angiogenesis receptor tyrosine kinase
846 inhibitors in cancer therapy. J Hematol Oncol. 2019; 12: 27.
847 44. Ferrara N. VEGF as a Therapeutic Target in Cancer. Oncology. 2005; 69: 11-6.
848 45. Lopes-Coelho F, Martins F, Pereira SA, Serpa J. Anti-angiogenic therapy: current challenges and future
849 perspectives. International Journal of Molecular Sciences; 2021.
850 46. Hu H, Chen Y, Tan S, Wu S, Huang Y, Fu S, et al. The research progress of antiangiogenic therapy, immune
851 therapy and tumor microenvironment. Front Immunol. 2022; 13: 802846.
852 47. Faivre S, Demetri G, Sargent W, Raymond E. Molecular basis for sunitinib efficacy and future clinical
853 development. Nature Reviews Drug Discovery. 2007; 6: 734-45.
854 48. Motzer RJ, Hoosen S, Bello CL, Christensen JG. Sunitinib malate for the treatment of solid tumours: a review
855 of current clinical data. Expert Opin Investig Drugs. 2006; 15: 553-61.
856 49. Gaustad JV, Simonsen TG, Wegner CS, Rofstad EK. Vascularization, oxygenation, and the effect of sunitinib
857 treatment in pancreatic ductal adenocarcinoma xenografts. Front Oncol. 2019; 9: 845.
858 50. Welti JC, Powles T, Foo S, Gourlaouen M, Preece N, Foster J, et al. Contrasting effects of sunitinib within in
859 vivo models of metastasis. Angiogenesis. 2012; 15: 623-41.
860 51. Matsumoto S, Batra S, Saito K, Yasui H, Choudhuri R, Gadisetti C, et al. Antiangiogenic agent sunitinib
861 transiently increases tumor oxygenation and suppresses cycling hypoxia. Cancer Res. 2011; 71: 6350-9.

862 52. Yadav K, Lim J, Choo J, Ow SGW, Wong A, Lee M, et al. Immunohistochemistry study of tumor vascular
863 normalization and anti-angiogenic effects of sunitinib versus bevacizumab prior to dose-dense
864 doxorubicin/cyclophosphamide chemotherapy in HER2-negative breast cancer. Breast Cancer Research and
865 Treatment. 2022; 192: 131-42.
866 53. Xin H, Zhang C, Herrmann A, Du Y, Figlin R, Yu H. Sunitinib inhibition of Stat3 induces renal cell carcinoma
867 tumor cell apoptosis and reduces immunosuppressive cells. Cancer Research. 2009; 69: 2506-13.
868 54. Wang B, Lu D, Xuan M, Hu W. Antitumor effect of sunitinib in human prostate cancer cells functions via
869 autophagy. Exp Ther Med. 2017; 13: 1285-94.
870 55. Tran Cao HS, Bouvet M, Kaushal S, Keleman A, Romney E, Kim G, et al. Metronomic gemcitabine in
871 combination with sunitinib inhibits multisite metastasis and increases survival in an orthotopic model of pancreatic
872 cancer. Molecular Cancer Therapeutics. 2010; 9: 2068-78.
873 56. Ocadlikova D, Lecciso M, Broto JM, Scotlandi K, Cavo M, Curti A, et al. Sunitinib exerts in vitro
874 immunomodulatory activity on sarcomas via dendritic cells and synergizes with PD-1 blockade. Front Immunol. 2021;
875 12: 577766.
876 57. Motzer RJ, Hutson TE, Tomczak P, Michaelson MD, Bukowski RM, Rixe O, et al. Sunitinib versus Interferon
877 Alfa in Metastatic Renal-Cell Carcinoma. New England Journal of Medicine. 2007; 356: 115-24.
878 58. Motzer RJ, Hutson TE, Tomczak P, Michaelson MD, Bukowski RM, Oudard S, et al. Overall survival and
879 updated results for sunitinib compared with interferon alfa in patients with metastatic renal cell carcinoma. J Clin
880 Oncol. 2009; 27: 3584-90.
881 59. Li W, Zhan M, Quan Y-y, Wang H, Hua S-n, Li Y, et al. Modulating the tumor immune microenvironment
882 with sunitinib malate supports the rationale for combined treatment with immunotherapy. International
883 Immunopharmacology. 2020; 81: 106227.
884 60. Korashy HM, Maayah ZH, Al Anazi FE, Alsaad AM, Alanazi IO, Belali OM, et al. Sunitinib inhibits breast
885 cancer cell proliferation by inducing apoptosis, cell-cycle arrest and DNA repair while inhibiting NF-kappaB signaling
886 pathways. Anticancer Res. 2017; 37: 4899-909.
887 61. Kleibeuker EA, Ten Hooven MA, Verheul HM, Slotman BJ, Thijssen VL. Combining radiotherapy with
888 sunitinib: lessons (to be) learned. Angiogenesis. 2015; 18: 385-95.
889 62. Gaustad J-V, Simonsen TG, Andersen LMK, Rofstad EK. Antiangiogenic agents targeting different
890 angiogenic pathways have opposite effects on tumor hypoxia in R-18 human melanoma xenografts. BMC Cancer.
891 2017; 17: 411.
892 63. Fu SY, Wang CC, Chen FH, Yu CF, Hong JH, Chiang CS. Sunitinib treatment-elicited distinct tumor
893 microenvironment dramatically compensated the reduction of myeloid-derived suppressor Cells. In Vivo. 2020; 34:
894 1141-52.
895 64. Faivre S, Delbaldo C, Vera K, Robert C, Lozahic S, Lassau N, et al. Safety, pharmacokinetic, and antitumor
896 activity of SU11248, a novel oral multitarget tyrosine kinase inhibitor, in patients with cancer. J Clin Oncol. 2006; 24:
897 25-35.
898 65. Demetri GD, van Oosterom AT, Garrett CR, Blackstein ME, Shah MH, Verweij J, et al. Efficacy and safety
899 of sunitinib in patients with advanced gastrointestinal stromal tumour after failure of imatinib: a randomised controlled
900 trial. Lancet. 2006; 368: 1329-38.
901 66. Cuneo KC, Geng L, Fu A, Orton D, Hallahan DE, Chakravarthy AB. SU11248 (sunitinib) sensitizes
902 pancreatic cancer to the cytotoxic effects of ionizing radiation. International Journal of Radiation
903 Oncology*Biology*Physics. 2008; 71: 873-9.
904 67. Conley SJ, Gheordunescu E, Kakarala P, Newman B, Korkaya H, Heath AN, et al. Antiangiogenic agents
905 increase breast cancer stem cells via the generation of tumor hypoxia. Proceedings of the National Academy of
906 Sciences. 2012; 109: 2784-9.
907 68. Casneuf VF, Delrue L, Van Damme N, Demetter P, Robert P, Corot C, et al. Noninvasive monitoring of
908 therapy-induced microvascular changes in a pancreatic cancer model using dynamic contrast-enhanced magnetic
909 resonance imaging with P846, a new low-diffusible gadolinium-based contrast agent. Radiation Research. 2010; 175:
910 10-20.
911 69. Awasthi N, Zhang C, Schwarz AM, Hinz S, Schwarz MA, Schwarz RE. Enhancement of nab-paclitaxel
912 antitumor activity through addition of multitargeting antiangiogenic agents in experimental pancreatic cancer.
913 Molecular Cancer Therapeutics. 2014; 13: 1032-43.
914 70. Payne LB, Hoque M, Houk C, Darden J, Chappell JC. Pericytes in vascular development. Curr Tissue
915 Microenviron Rep. 2020; 1: 143-54.
916 71. Ferland-McCollough D, Slater S, Richard J, Reni C, Mangialardi G. Pericytes, an overlooked player in
917 vascular pathobiology. Pharmacol Ther. 2017; 171: 30-42.

72. Mendel DB, Laird AD, Xin X, Louie SG, Christensen JG, Li G, et al. In vivo antitumor activity of SU11248, a novel tyrosine kinase inhibitor targeting vascular endothelial growth factor and platelet-derived growth factor receptors: determination of a pharmacokinetic/pharmacodynamic relationship. Clinical Cancer Research. 2003; 9: 327-37.
73. List of targeted therapy drugs approved for specific types of cancer. National Cancer Institute: National Institute of Health.
74. Wang LV, Yao J. A practical guide to photoacoustic tomography in the life sciences. Nat Methods. 2016; 13: 627-38.
75. Beard P. Biomedical photoacoustic imaging. Interface Focus. 2011; 1: 602-31.
76. Luke GP, Yeager D, Emelianov SY. Biomedical applications of photoacoustic imaging with exogenous contrast agents. Ann Biomed Eng. 2012; 40: 422-37.
77. Lin L, Wang LV. The emerging role of photoacoustic imaging in clinical oncology. Nat Rev Clin Oncol. 2022.
78. Kim J, Lee D, Jung U, Kim C. Photoacoustic imaging platforms for multimodal imaging. Ultrasonography. 2015; 34: 88-97.
79. Han S, Lee D, Kim S, Kim HH, Jeong S, Kim J. Contrast agents for photoacoustic imaging: a review focusing on the wavelength range. Biosensors (Basel). 2022; 12.
80. Yao J, Wang LV. Sensitivity of photoacoustic microscopy. Photoacoustics. 2014; 2: 87-101.
81. Li M, Tang Y, Yao J. Photoacoustic tomography of blood oxygenation: a mini review. Photoacoustics. 2018; 10: 65-73.
82. Claus A, Sweeney A, Sankepalle DM, Li B, Wong D, Xavierselvan M, et al. 3D Ultrasound-guided photoacoustic imaging to monitor the effects of suboptimal tyrosine kinase inhibitor therapy in pancreatic tumors. Front Oncol. 2022; 12: 915319.
83. Mallidi S, Watanabe K, Timerman D, Schoenfeld D, Hasan T. Prediction of tumor recurrence and therapy monitoring using ultrasound-guided photoacoustic imaging. Theranostics. 2015; 5: 289-301.
84. Hysi E, Wirtzfeld LA, May JP, Undzys E, Li SD, Kolios MC. Photoacoustic signal characterization of cancer treatment response: Correlation with changes in tumor oxygenation. Photoacoustics. 2017; 5: 25-35.
85. Haedicke K, Agemy L, Omar M, Berezhnoi A, Roberts S, Longo-Machado C, et al. High-resolution optoacoustic imaging of tissue responses to vascular-targeted therapies. Nat Biomed Eng. 2020; 4: 286-97.
86. Bosari S, Lee AKC, DeLellis RA, Wiley BD, Heatley GJ, Silverman ML. Microvessel quantitation and prognosis in invasive breast carcinoma. Human Pathology. 1992; 23: 755-61.
87. Hlatky L, Hahnfeldt P, Folkman J. Clinical application of antiangiogenic therapy: microvessel density, what it does and doesn't tell us. JNCI: Journal of the National Cancer Institute. 2002; 94: 883-93.
88. Schoell WMJ, Pieber D, Reich O, Lahousen M, Janicek M, Guecer F, et al. Tumor angiogenesis as a prognostic factor in ovarian carcinoma. Cancer. 1997; 80: 2257-62.
89. Yoshino S, Kato M, Okada K. Prognostic significance of microvessel count in ow stage renal cell carcinoma. International Journal of Urology. 1995; 2.
90. Marien KM, Croons V, Waumans Y, Sluydts E, De Schepper S, Andries L, et al. Development and validation of a histological method to measure microvessel density in whole-slide images of cancer tissue. PLoS One. 2016; 11: e0161496.
91. Zhao J, Zhao Q, Lin R, Meng J. A microvascular image analysis method for optical-resolution photoacoustic microscopy. Journal of Innovative Optical Health Sciences. 2020; 13.
92. Sun M, Li C, Chen N, Zhao H, Ma L, Liu C, et al. Full three-dimensional segmentation and quantification of tumor vessels for photoacoustic images. Photoacoustics. 2020; 20: 100212.
93. Yang Z, Chen J, Yao J, Lin R, Meng J, Liu C, et al. Multi-parametric quantitative microvascular imaging with optical-resolution photoacoustic microscopy in vivo. Opt Express. 2014; 22: 1500-11.
94. Sciortino VM, Tran A, Sun N, Cao R, Sun T, Sun YY, et al. Longitudinal cortex-wide monitoring of cerebral hemodynamics and oxygen metabolism in awake mice using multi-parametric photoacoustic microscopy. J Cereb Blood Flow Metab. 2021; 41: 3187-99.
95. Zhao H, Huang J, Zhou Q, Chen N, Liu L, Wang X, et al. Deep learning-based optical-resolution photoacoustic microscopy for in vivo 3D microvasculature imaging and segmentation. Advanced Intelligent Systems. 2022; 4: 2200004.
96. Yeh C, Soetikno B, Hu S, Maslov KI, Wang LV. Microvascular quantification based on contour-scanning photoacoustic microscopy. J Biomed Opt. 2014; 19: 96011.
97. Oraevsky AA, Soetikno B, Hu S, Gonzales E, Zhong Q, Maslov K, et al. Vessel segmentation analysis of ischemic stroke images acquired with photoacoustic microscopy. Photons Plus Ultrasound: Imaging and Sensing 2012; 2012.

98. Mai TT, Yoo SW, Park S, Kim JY, Choi K-H, Kim C, et al. In vivo quantitative vasculature segmentation and assessment for photodynamic therapy process monitoring using photoacoustic microscopy. Sensors; 2021.
99. Ly CD, Nguyen VT, Vo TH, Mondal S, Park S, Choi J, et al. Full-view in vivo skin and blood vessels profile segmentation in photoacoustic imaging based on deep learning. Photoacoustics. 2022; 25: 100310.
100. Brown EL, Lefebvre TL, Sweeney PW, Stolz BJ, Grohl J, Hacker L, et al. Quantification of vascular networks in photoacoustic mesoscopy. Photoacoustics. 2022; 26: 100357.
101. Ntziachristos V. Going deeper than microscopy: the optical imaging frontier in biology. Nat Methods. 2010; 7: 603-14.
102. Yao J, Wang LV. Photoacoustic brain imaging: from microscopic to macroscopic Scales. Neurophotonics. 2014; 1.
103. Fang Q, Boas DA. Monte Carlo simulation of photon migration in 3D turbid media accelerated by graphics processing units. Opt Express. 2009; 17: 20178–90.
104. Yan S, Jacques SL, Ramella-Roman JC, Fang Q. Graphics-processing-unit-accelerated Monte Carlo simulation of polarized light in complex three-dimensional media. J Biomed Opt. 2022; 27.
105. Sweeney A, Arora A, Edwards SA, Mallidi S. Ultrasound-guided Photoacoustic image annotation toolkit in MATLAB (PHANTOM) for preclinical applications. Photoacoustics. 2024: 100662.
106. Otsu N. A Threshold selection method from gray-level histograms. IEEE Transactions on Systems, Man, and Cybernetics. 1979; 9: 62-6.
107. Jumiawi WAH, El-Zaart A. Improvement in the between-class variance based on lognormal distribution for accurate image segmentation. Entropy; 2022.
108. Xavierselvan M, Singh MKA, Mallidi S. In vivo tumor vascular imaging with light emitting diode-based photoacoustic imaging system. Sensors. 2020; 20: 4503.
109. Vercauteren T, Pennec X, Perchant A, Ayache N. Diffeomorphic demons: efficient non-parametric image registration. Neuroimage. 2009; 45: S61-72.
110. Thirion JP. Image matching as a diffusion process: an analogy with Maxwell's demons. Medical Image Analysis. 1998; 2: 243-60.
111. Tien YW, Wu YM, Lin WC, Lee HS, Lee PH. Pancreatic carcinoma cells stimulate proliferation and matrix synthesis of hepatic stellate cells. J Hepatol. 2009; 51: 307-14.
112. Miknyocski SJ, Chang H, Klein-Szanto A, Dionne CA, Ruggeri BA. The Trk tyrosine kinase inhibitor CEP-701 (KT-5555) exhibits significant antitumor efficacy in preclinical xenograft models of human pancreatic ductal adenocarcinoma. Clin Cancer Res. 1999; 5: 2205-12.
113. Scholzen T, Gerdes J. The Ki-67 protein: From the known and the unknown. Journal of Cellular Physiology. 2000; 182: 311-22.
114. Liang Y, Sheng G, Guo Y, Zou Y, Guo H, Li Z, et al. Prognostic significance of grade of malignancy based on histopathological differentiation and Ki-67 in pancreatic ductal adenocarcinoma. Cancer Biology & Medicine. 2024: 20230363.
115. Myoteri D, Dellaportas D, Lykoudis PM, Apostolopoulos A, Marinis A, Zizi-Sermpetzoglou A. Prognostic evaluation of vimentin expression in correlation with Ki67 and CD44 in surgically resected pancreatic ductal adenocarcinoma. Gastroenterology Research and Practice. 2017; 2017: 9207616.
116. Pergolini I, Crippa S, Pagnanelli M, Belfiori G, Pucci A, Partelli S, et al. Prognostic impact of Ki-67 proliferative index in resectable pancreatic ductal adenocarcinoma. BJS Open. 2019; 3: 646-55.
117. Linder S, Parrado C, Falkmer UG, Blåsjö M, Sundelin P, von Rosen A. Prognostic significance of Ki-67 antigen and p53 protein expression in pancreatic duct carcinoma: a study of the monoclonal antibodies MIB-1 and DO-7 in formalin-fixed paraffin-embedded tumour material. British Journal of Cancer. 1997; 76: 54-9.
118. Karamitopoulou E, Zlobec I, Tornillo L, Carafa V, Schaffner T, Brunner T, et al. Differential cell cycle and proliferation marker expression in ductal pancreatic adenocarcinoma and pancreatic intraepithelial neoplasia (PanIN). Pathology. 2010; 42: 229-34.
119. Tomaszewski MR, Gonzalez IQ, O'Connor JP, Abeyakoon O, Parker GJ, Williams KJ, et al. Oxygen enhanced optoacoustic tomography (OE-OT) reveals vascular dynamics in murine models of prostate cancer. Theranostics. 2017; 7: 2900-13.
120. Bohndiek SE, Sasportas LS, Machtaler S, Jokerst JV, Hori S, Gambhir SS. Photoacoustic tomography detects early vessel regression and normalization during ovarian tumor response to the antiangiogenic therapy trebananib. Journal of Nuclear Medicine. 2015; 56: 1942-7.
121. Wey JS, Fan F, Gray MJ, Bauer TW, McCarty MF, Somcio R, et al. Vascular endothelial growth factor receptor-1 promotes migration and invasion in pancreatic carcinoma cell lines. Cancer. 2005; 104: 427-38.

122. Liang C, Yuan X, Shen Z, Wang Y, Ding L. Vorolanib, a novel tyrosine receptor kinase receptor inhibitor with potent preclinical anti-angiogenic and anti-tumor activity. Mol Ther Oncolytics. 2022; 24: 577-84.
123. Robertson RT, Levine ST, Haynes SM, Gutierrez P, Baratta JL, Tan Z, et al. Use of labeled tomato lectin for imaging vasculature structures. Histochem Cell Biol. 2015; 143: 225-34.
124. Raumonen P, Tarvainen T. Segmentation of vessel structures from photoacoustic images with reliability assessment. Biomed Opt Express. 2018; 9: 2887-904.
125. Huangxuan Z, Guangsong W, Riqiang L, Xiaojing G, Liang S, Tan L, et al. Three-dimensional Hessian matrix-based quantitative vascular imaging of rat iris with optical-resolution photoacoustic microscopy in vivo. Journal of Biomedical Optics. 2018; 23: 046006.
126. Oruganti T, Oraevsky AA, Laufer JG, Wang LV, Treeby BE. Vessel filtering of photoacoustic images. Photons Plus Ultrasound: Imaging and Sensing 2013; 2013.
127. Paul WS, Lina H, Thierry LL, Emma LB, Janek G, Sarah EB. Unsupervised segmentation of 3D microvascular photoacoustic images using deep generative learning. bioRxiv. 2024: 2023.04.30.538453.
128. Vaiyapuri T, Dutta AK, Sikkandar MY, Gupta D, Alouffi B, Alharbi A, et al. Design of metaheuristic optimization-based vascular segmentation techniques for photoacoustic images. Contrast Media Mol Imaging. 2022; 2022: 4736113.
129. Le TD, Kwon S-Y, Lee C. Segmentation and quantitative analysis of photoacoustic imaging: a review. Photonics. 2022; 9.
130. Sorensen BS, Horsman MR. Tumor hypoxia: impact on radiation therapy and molecular pathways. Front Oncol. 2020; 10: 562.
131. Hong L, Li J, Luo Y, Guo T, Zhang C, Ou S, et al. Recent advances in strategies for addressing hypoxia in tumor photodynamic therapy. Biomolecules. 2022; 12.
132. Ferrara N. Role of vascular endothelial growth factor in the regulation of angiogenesis. Kidney Int. 1999; 56: 794-814.
133. Xin X, Yang S, Ingle G, Zlot C, Rangell L, Kowalski J, et al. Hepatocyte growth factor enhances vascular endothelial growth factor-induced angiogenesis in vitro and in vivo. Am J Pathol. 2001; 158: 1111-20.
134. Hiratsuka S, Minowa O, Kuno J, Noda T, Shibuya M. Flt-1 lacking the tyrosine kinase domain is sufficient for normal development and angiogenesis in mice. Proc Natl Acad Sci USA. 1998; 95: 9349-54.
135. Meyers RM, Bryan JG, McFarland JM, Weir BA, Sizemore AE, Xu H, et al. Computational correction of copy number effect improves specificity of CRISPR-Cas9 essentiality screens in cancer cells. Nat Genet. 2017; 49: 1779-84.
136. Dempster JM, Rossen J, Kazachkova M, Pan J, Kugener G, Root DE, et al. Extracting biological insights from the Project Achilles genome-scale CRISPR screens in cancer cell lines. 2019.
137. Deer EL, Gonzalez-Hernandez J, Coursen JD, Shea JE, Ngatia J, Scaife CL, et al. Phenotype and genotype of pancreatic cancer cell lines. Pancreas. 2010; 39: 425-35.
138. Luo J, Guo P, Matsuda K, Truong N, Lee A, Chun C, et al. Pancreatic cancer cell-derived vascular endothelial growth factor is biologically active in vitro and enhances tumorigenicity in vivo. International Journal of Cancer. 2001; 92: 361-9.
139. Benjamin LE, Golijanin D, Itin A, Pode D, Keshet E. Selective ablation of immature blood vessels in established human tumors follows vascular endothelial growth factor withdrawal. The Journal of Clinical Investigation. 1999; 103: 159-65.
140. Fleming JB, Brekken RA. Functional imaging of angiogenesis in an orthotopic model of pancreatic cancer. Journal of Cellular Biochemistry. 2003; 90: 492-501.
141. Andersen LMK, Wegner CS, Simonsen TG, Huang R, Gaustad JV, Hauge A, et al. Lymph node metastasis and the physicochemical micro-environment of pancreatic ductal adenocarcinoma xenografts. Oncotarget. 2017; 8: 48060-74.